# A novel multifunctional magnetically recyclable BiOBr/ZnFe$_2$O$_4$-GO S-scheme ternary heterojunction: Photothermal synergistic catalysis under Vis/NIR light and NIR-driven photothermal detection of tetracycline

Sicheng Cui [a], Yuan Cong [a], Wenshi Zhao [a,b,c], Rui Guo [a], Xiaohan Wang [a], Bohui Lv [a], Hongbo Liu [a], Yang Liu [a,*], Qi Zhang [a,*]

[a] Key Laboratory of Functional Materials Physics and Chemistry of the Ministry of Education, Jilin Normal University, Changchun 130103, China
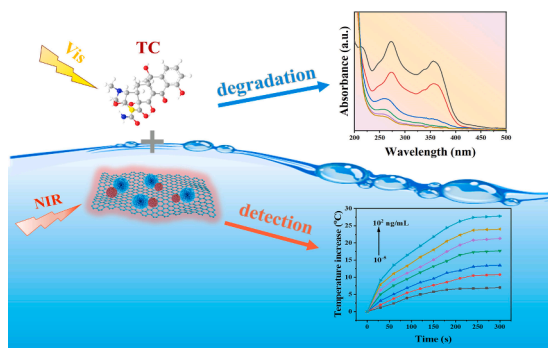[b] Changchun Institute of Optics, Fine Mechanics and Physics, Chinese Academy of Sciences, Changchun 130033, China
[c] University of Chinese Academy of Sciences, Beijing 100049, China

## HIGHLIGHTS

- A novel BiOBr/ZnFe$_2$O$_4$-GO S-scheme heterojunction was successfully constructed.
- The effect of GO content on catalytic activity of BOB/ZFO-GO NCs was investigated.
- BOB/ZFO-GO NCs achieved photothermal synergistic catalysis for TC.
- The mechanism of BOB/ZFO-GO NCs catalytic degradation for TC was analyzed.
- Photothermal detection sensor has a detection limit as low as $10^{-4}$ ng/mL for TC.

## GRAPHICAL ABSTRACT



## ARTICLE INFO

## ABSTRACT

The threat of tetracycline (TC) to human health has become a significant issue that cannot be disregarded. Herein, in order to achieve effective degradation and high-sensitivity detection of TC, BiOBr/ZnFe$_2$O$_4$-GO (BOB/ ZFO-GO) S-scheme heterojunction nanocomposites (NCs) have been prepared using hydrothermal method. GO with high light absorption capacity accelerated the electron transfer between BiOBr and ZnFe$_2$O$_4$ nanocrystals and extended the light absorption region of BOB/ZFO NCs. The optimal GO addition of BOB/ZFO-GO NCs could degrade TC solution of 10 mg/L in 80 min and have a high reaction rate constant (k) of 0.072 min$^{-1}$ under visible/NIR light. According to calculations, the non-metal photocatalyst (BOB/ZFO-GO(2)) with the best degradation performance had a photothermal conversion efficiency of up to 23%. Meanwhile, BOB/ZFO-GO NCs could be recycled by magnetic field. The excellent photocatalytic and photothermal performance could be maintained even after several cycles. In addition, a photothermal detection sensor based on a photothermal material/specific recognition element/tetracycline sandwich-type structure was constructed for the trace detection of TC concentration with a detection limit as low as $10^{-4}$ ng/mL. This research provides a unique idea

---

\* Corresponding authors.
*E-mail addresses:* liuyang@jlnu.edu.cn (Y. Liu), qzh7512@126.com (Q. Zhang).

for the multi-functionalization of photocatalysts and has a wide range of potential applications for the identification and treatment of organic wastewater.

## 1. Introduction

Currently, with the intensification of environmental pollution, water pollution has become the most concerned focus of society, which is also a global problem to be solved [1]. Antibiotics, as one of the important drugs in the medical field, can prevent and treat diseases caused by bacterial infections by inhibiting the growth and reproduction of pathogenic microorganisms [2,3]. However, the antibiotics taken by humans or animals cannot be completely absorbed, and thus large amounts of antibiotics are released into the environment in the form of antibiotic metabolites or even unchanged antibiotics [4]. Furthermore, the use of antibiotics usually causes antibiotic resistance in pathogenic microorganisms, and hence the effective dosages of antibiotics that can kill bacteria need to be continuously increased [5]. More unfortunately, the production of antibiotic-resistant genes in the environment will further aggravate the risk of spread of antibiotic resistance [6]. Hence, antibiotics are one of the main sources of environmental pollution. Among the various antibiotics commonly used in clinical, tetracycline (TC), being a typical broad-spectrum antibiotic, is already the second widest-used antibiotic in the world due to its low price, strong bacteriostasis and stable structure [7,8]. Nevertheless, the excessive use of TC can lead to its continuous accumulation in the ecosystem, and ultimately get into the human body by way of the food cycle and drinking water, which will cause serious health hazards such as liver poisoning, intestinal dysfunction and allergic reaction [9–11]. Worst of all, even at trace levels, TC can also provoke leukopenia, stomatitis and other diseases [12]. Accordingly, it is necessary and eager to establish a valid method for the high-sensitivity determination and efficient removal of TC in the aquatic environment.

At present, various methods have been developed to remove TC from aqueous environment, including physical adsorption, anaerobic biodegradation and electrochemical reaction [13]. Although these methods have their own merits, they also have certain limitations. For instance, the physical adsorption method has the advantage of simple operation, but it only transfers the TC to adsorbent, which cannot fundamentally solve the problem of TC pollution [14]. Anaerobic biodegradation is a low cost and environmentally friendly technology, but it cannot completely degrade antibiotic residues in wastewater, and the remaining antibiotic may be adsorbed by sludge [15]. Electrochemical reaction is very effective in removing organic pollutants, however, the process of achieving complete mineralization requires very high energy consumption, which seriously limits its practical application [16]. In recent years, photocatalytic technology has attracted much attention in the field of pollutant degradation [17]. Unlike traditional techniques, photocatalytic technology can achieve the direct conversion of light energy to chemical energy and promote the decomposition of organic matter, which has the advantages of eco-friendliness, energy saving, high effectiveness and economic benefits, and is considered the most prospective method for degradation of TC [18,19]. The design and construction of photocatalysts with high catalytic activities will be critical to achieve the practical application of this technology [20]. Bismuth halide oxides (BiOX, X = I, Br, Cl) are recognized as important photocatalyst candidates because of their remarkable visible light response and distinctive electronic structure [21]. BiOBr, in particular, has recently drawn more interests owing to its suitable bandgap (~2.6 eV), good adsorption capacity for diverse organic pollutants and high visible light absorption capacity [22,23]. However, the high recombination of the photogenerated electrons (e$^-$) and holes (h$^+$) of BiOBr monomer results in its low photocatalytic activity [24,25]. Moreover, the prepared BiOBr photocatalysts usually exist in the form of powders, which will be detrimental to the recycling and reuse after catalytic

degradation process, and even cause secondary pollution to the water environment [26]. In order to improve the photocatalytic activity of BiOBr and realize the recycling of BiOBr, the combination of BiOBr and magnetic semiconductor with the suitable energy bandgap has proven to be the most effective solution [27]. $ZnFe_2O_4$ is a widely known spinel ($AB_2O_4$) magnetic semiconductor with a narrow energy bandgap (~1.9 eV) and a wide range of optical responses, which is also a prospective magnetic photocatalyst [28,29]. More importantly, a large number of studies have shown that the combination of $ZnFe_2O_4$ and BiOBr can construct a S-scheme heterojunction, and spatial separation of photo-generated carriers can be achieved while maintaining the strongest redox capability [30,31]. Therefore, the combination of $ZnFe_2O_4$ and BiOBr can not only fully utilize photogenerated charge carriers and significantly enhance the photocatalytic performance, but also remove and recycle the photocatalyst powder through an external magnetic field.

At present, much research have been devoted to the photocatalytic degradation of antibiotics using BiOBr/$ZnFe_2O_4$ nanocomposites (BOB/ZFO NCs) as photocatalysts. For example, Wang et al. synthesized $ZnFe_2O_4$/$Bi_2O_2CO_3$/BiOBr double Z-scheme heterojunctions photocatalysts and achieved degradation for TC under visible light [32]. Chen et al. prepared a novel polyvinylpyrrolidone biochar@$ZnFe_2O_4$/BiOBr heterojunction photocatalyst to eliminate ciprofloxacin from wastewater [33]. However, BOB/ZFO NCs photocatalysts only absorb energy in the visible light range in the process of degradation. Given that visible light only makes up about 45% of sunlight, the full utilization of solar energy is another key factor to be considered during photocatalytic process [34,35]. To extend the optical absorption range of BOB/ZFO NCs from visible light to near-infrared (NIR) light (~50 % of solar energy), a workable solution is to combine graphene oxide (GO) with NIR light absorption ability with BOB/ZFO NCs [36,37]. Another advantage of GO is that GO with sufficiently high surface area and rich oxidized functional groups can act as both a carrier of BOB/ZFO NCs and an electron transfer channel to capture and transfer the excited electrons [38,39]. More importantly, BOB/ZFO-GO can utilize the full-spectrum sunlight absorption ability of GO to produce photothermal effects, and thus increase the local temperature around BOB/ZFO-GO based on thermal vibration mechanism under NIR light irradiation, which will accelerate the transfer of the excited electrons and further enhance photocatalytic performance [40,41].

In fact, BOB/ZFO-GO can not only achieve efficient degradation of TC, but also be used for quantitative detection of trace TC residues in wastewater due to the photothermal effects of GO. Currently, there are common methods used to analyze and detect antibiotics including liquid chromatography, capillary electrophoresis, enzyme-linked immunosorbent assay and microbial screening method [42–45]. Nevertheless, such techniques usually require time-consuming and cumbersome pretreatment procedures for samples, or have the disadvantage of low sensitivity and stability [46,47]. A photothermal detection method based on the photothermal property of BOB/ZFO-GO can well overcome the above disadvantages [48]. In photothermal detection, no sophisticated precision instrumentation is required, and quantitative signals can be achieved only using an ordinary thermometer or infrared camera [49,50]. One problem that needs to be solved is to bind TC to BOB/ZFO-GO NCs and set the target concentration as a function of temperature change [51]. In recent years, many specific recognition elements, such as antibodies, enzymes and aptamers (Apt), have been used to bind target molecules [52]. Among them, Apt has attracted much attention because of its simplicity, practicality and cheapness [53,54]. Apt is a thermally stable short single nucleotide chain with unique sequence structure and a broad range of specific target binding capabilities that

can be synthesized in large quantities in vitro [55,56]. The TC-specific Apt has a strong binding affinity to TC, which can act as a bridge between the BOB/ZFO-GO and TC to form an Apt-BOB/ZFO-GO/TC sandwich structure [57,58]. This sandwich structure can release heat due to the photothermal effect of BOB/ZFO-GO under NIR irradiation, and thus raise the solution temperature [59]. It can be observed that the temperature rise is proportional to the TC concentration, thus establishing a quantitative relationship between the temperature signal and TC concentration [60]. To our knowledge, such studies combining photothermal catalysis with photothermal detection have never been reported in the literature.

In this paper, a novel BOB/ZFO-GO S-scheme heterojunction with dual functions of catalytic degradation and concentration detection has been designed and constructed. The influence of GO addition on photocatalytic performance of BOB/ZFO NCs was investigated. It was also confirmed that the photothermal effect, which was often overlooked, promoted photocatalysis. Meanwhile, the charge transfer mechanism of BOB/ZFO-GO S-scheme heterojunction and the corresponding photocatalytic mechanism for TC were analyzed and discussed. Due to the presence of $ZnFe_2O_4$ nanocrystals, BOB/ZFO-GO NCs could be quickly recycled through the application of magnetic fields. In addition, based on the photothermal property of the BOB/ZFO-GO NCs, we constructed a photothermal detection sensor and developed a sandwich structure consisting of TC, Apt and BOB/ZFO-GO NCs. The apt-modified BOB/ZFO-GO NCs could specifically bind to TC molecules and cause a visible temperature change under NIR light irradiation. The temperature rise became more pronounced as TC concentration increased. The positive correlation between temperature change and TC concentration was used to achieve quantitative detection of TC concentration. Multifunctional BOB/ZFO-GO NCs are anticipated to have wide applied prospects on the removal and detection for antibiotic contamination.

## 2. Experimental section

### 2.1. Chemicals

Bismuth nitrate pentahydrate ($Bi(NO_3)_3 \cdot 5H_2O$), zinc acetate dihydrate ($Zn(CH_3COO)_2 \cdot 2H_2O$), isopropyl alcohol (IPA) and glycerine (GI) were obtained from Shanghai Macklin Biochemical Co., Ltd. (Shanghai, China). Ethylene glycol (EG), graphite powder, sulfuric acid ($H_2SO_4$), ferric nitrate ninhydrate ($Fe(NO_3)_3 \cdot 9H_2O$), boric acid ($H_3PO_4$) and potassium permanganate ($KMn_2O_4$) were purchased from Aladdin Reagent Co., Ltd. (Shanghai, China). 1-(3-(dimethyl aminopropyl)-3-ethyl carbodiimide hydrochloride (EDC), and bovine serum albumin (BSA) were supplied from J&K Chemical Co. Hydrogen, hydrogen peroxide ($H_2O_2$), p-benzoquinone (BQ), triethanolamine (TEOA), sodium sulfate ($Na_2SO_4$), potassium bromide (KBr), *N*-hydroxysuccinimide (NHS), polyvinyl, pyrrolidone (PVP), oleic acid, absolute ethanol and TC were received from Sinopharm Chemical Reagent Co., Ltd. All reagents employed in the present study were of analytical grade and did not require further purification.

Shanghai Sangon Biological Science & Technology Company (Shanghai, China) synthesized an Apt that could specifically recognize TC with the sequence of 15′–NH₂-GAGCUCAGCCUGUA-CUGCUGCUUAAAGCCUAAAACAUACCA-GAUCGCCACCCGCGCUUUAAUCUGGAGAGGUGAA-GAAUUCGACCACCUAGGCUGCACCACGG-3′ [61].

### 2.2. Synthesis of BOB/ZFO binary NCs

As shown in Scheme 1(a), $ZnFe_2O_4$ nanocrystals were synthesized by a simple hydrothermal method [62]. In an usual process, 0.808 g of Fe($NO_3$)$_3$·9H$_2$O and 0.2195 g of Zn(CH$_3$COO)$_2$·2H$_2$O were dispersed into a mixed solution containing 30 mL of IPA and 8 mL of GI with magnetic stirring for 40 min. Subsequently, the above blend was moved to Teflon-
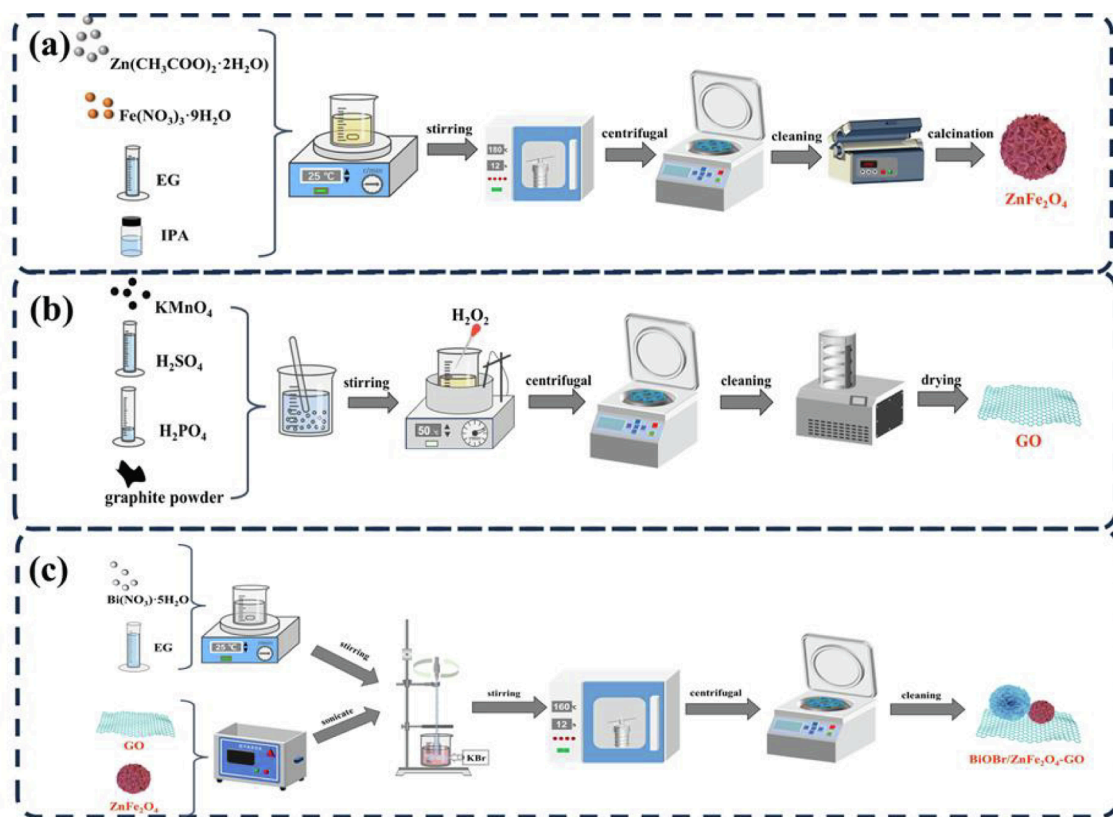


**Scheme 1.** Schematic illustration of the synthesis procedure of (a) $ZnFe_2O_4$ nanocrystals, (b) GO and (c) BOB/ZFO-GO NCs.

lined stainless-steel autoclave and reacted at 180 °C for 12 h. After cooling naturally until room temperature, the collected precipitate was centrifugally washed by repeated use of deionized water and ethanol, and then left to dry at 60 °C for 8 h. After that, the powder obtained after drying was put into a crucible and heated to 450 °C at an elevated temperature rate of 3 °C/min and held for 3 h. Finally, the powder cooled to room temperature was ground in a mortar and pestle to gain the $ZnFe_2O_4$ powder.

BOB/ZFO NCs were also synthesized via hydrothermal method [63]. Briefly, 0.7276 g of $Bi(NO_3)_3 \cdot 5H_2O$ and 0.0508 g of $ZnFe_2O_4$ were added into a beaker containing 16 mL EG and mechanically mixed for 1 h. Subsequently, 0.1786 g of KBr was added into the aforementioned mixture and kept stirring for another 2 h. The mixed solution was then moved to a stainless-steel autoclave. After incubation at 160 °C for 12 h, the resulting product was cooled and washed by centrifugation to obtain BOB/ZFO NCs. The prepared BOB/ZFO NCs were dried in air at 70 °C overnight. Pure BiOBr nanocrystals were also prepared according to a similar procedure, except that $ZnFe_2O_4$ nanocrystals were not added.

### 2.3. Synthesis of GO

GO was prepared via a modified Hummer's method based on natural graphite powder (Scheme 1(b)) [64]. Shortly, 1.5 g of graphite powder and 9 g of $KMn_2O_4$ were poured into the prepared 200 mL of the concentrated $H_2SO_4/H_3PO_4$ mixture ($V_{H_2SO_4} : V_{H_3PO_4} = 9:1$). After that, the mixture was put in the water bath at 50 °C with continuous stirring for 6 h. Next, $H_2O_2$ solution was added to the above mixture until the color was changed from black to orange and stirred continuously under heating conditions for 3 h. After that, the above mixture was cooled naturally and diluted with deionized water to adjust to pH = 6. Finally, the dried GO was acquired by centrifuging, washing and freezing.

### 2.4. Synthesis of BOB/ZFO-GO ternary NCs

As illustrated in Scheme 1(c), the synthesis process of BOB/ZFO-GO ternary NCs were described as follows: GO was added during the preparation of BOB/ZFO by hydrothermal method. The dried GO and $ZnFe_2O_4$ nanocrystals were added to a mixed solution containing $Bi(NO_3)_3 \cdot 5H_2O$ and EG under sonication. Then KBr was poured into the aforementioned mixture and mechanically stirred for 2 h. The other synthesis steps were the same as the previous method for preparing BOB/ZFO NCs, and the final BOB/ZFO-GO ternary NCs were gained by drying. The BOB/ZFO-GO ternary NCs with different GO mass contents of 1.0 wt%, 2.0 wt%, 3.0 wt% were named BOB/ZFO-GO(X), in which × represented the mass content of GO.

### 2.5. Synthesis of Apt-modified BOB/ZFO-GO NCs

The Apt-modified BOB/ZFO-GO NCs were prepared using the activated GO carboxyl interacting with the amino of Apt [65]. At first, the carboxyl was activated by adding 10 μL of EDC (100 mmol·L$^{-1}$) and 15 μL of NHS (100 mmol·L$^{-1}$) in 1 mL of BOB/ZFO-GO NCs and shaken for 2 h. After that, 10 μL of $NH_2$-Apt ($10^{-4}$ M) was added and the mixture was shaken at 240 rpm at 38 °C for 24 h. Finally, the results were collected with a magnetic iron and washed with PBS buffer to remove excess EDC and NHS, and the obtained Apt-modified BOB/ZFO-GO NCs were redispersed in PBS buffer containing 1% BSA and stored at 3 °C.

### 2.6. Characterization

The micromorphology and chemical structure of the as-prepared samples were analyzed by X-ray diffraction (XRD; Rigaku D/Max-2500), field-emission scanning electron microscopy (SEM; FEI Nova NanoSEM 450), fourier-transform infrared spectroscopy (FI-IR; IRTracer-100), transmission electron microscopy (TEM; JEOL 2100) and X-ray photoelectron spectroscopy (XPS; Thermo Scientific ESCALAB 250Xi). The specific surface area of the samples was studied by the Brunauer-Emmett-Teller (BET) method using nitrogen adsorption–desorption isotherms on a Micrometrics ASAP 2020 system. The photochemical and magnetic properties were investigated using a photoluminescence spectrum (PL; Hitachi F-4600), transient photocurrent response (CHI660E), diffuse reflectance spectra (DRS; LAMBDA950) and vibrating sample magnetometer (VSM; Lakeshore cryotronics 730). Ultraviolet–visible spectra were observed on a spectrophotometer (UV–Vis; Shimadzu UV3600). The temperature changes were recorded by thermal imaging camera (FOTRIC 326C-L44).

### 2.7. Photoelectrochemical measurements

The photoelectrochemical performance of the samples was analyzed by the CHI660E electrochemical workstation with a standard three-electrode system. The platinum wire, Ag/AgCl, and sample were selected for the counter electrode, the reference electrode and the working electrode, respectively. 0.5 mol·L$^{-1}$ of $Na_2SO_4$ aqueous solution was employed for electrolyte. 0.003 g of photocatalyst powder, 3 μL of anhydrous ethanol and oleic acid were mixed with 0.01 g of PVP. After ultrasonic mixing for 30 min to form a slurry, in order to make stronger adhesion uniformly coated on ITO glass, it is continuously heated at a constant high temperature for a few hours.

### 2.8. Photocatalytic experiments

The photocatalytic performance of the samples was studied by observing the degradation efficiency against TC solution at room temperature. 30 mg of catalyst powder was poured into 30 mL of TC solution (10 mg·L$^{-1}$). Photocatalytic experiments were all performed at room temperature. A mixture of 4 mL of catalyst and TC was extracted at fixed time intervals, and the change in concentration of TC was further observed using UV–Vis spectrum after filtering out the catalyst powder with a 0.22 mm filter tip.

### 2.9. Active substance capture experiments

Free radical trapping tests were conducted to determine the effect of free radicals on the photocatalytic reaction. In this way, the photocatalytic reaction mechanism was analyzed. BQ, IPA, and TEOA were employed to trap different reactive species, including superoxide radicals ($\bullet O^{2-}$), hydroxyl radicals ($\bullet OH$), and photogenerated holes ($h^+$), respectively. The free radical capture tests were performed according to the photocatalytic experiments except for the addition of the trapping agent.

### 2.10. NIR photothermal detection of TC residues in wastewater samples

To construct a photothermal detection sensing system, a sandwich structure based on specific binding of Apt and TC was constructed on 96-well plate. 150 μL of wastewater samples containing different concentrations ($10^{-4}$, $10^{-3}$, $10^{-2}$, $10^{-1}$, $10^0$, 10 and $10^2$ ng/mL) of TC were added to 96-well plate coating with TC-Apt and cultivated for 30 min at 38 °C. After washing, 40 μL of Apt-modified BOB/ZFO-GO NCs was added to a 96-well plate and cultivated at 38 °C for another 30 min [66]. Then the products were collected with magnet and washed for several times to remove unbound Apt-modified BOB/ZFO-GO NCs. Sequentially, the obtained Apt-BOB/ZFO-GO/TC complexes in the 96-well plate were irradiated under 808 nm laser (1.5 W cm$^{-2}$, spot 10 mm) for 300 s. The distance between the laser and the sample was kept around 7 cm, and then different concentrations of the solution were observed using a thermal imaging camera.

## 3. Results and discussion

### 3.1. Micromorphology and chemical structure

The phase purity of the synthesized samples was investigated using XRD technique. In Fig. 1(a), the diffraction peak (001) of GO emerges around 11.28° [67]. The diffraction patterns of $ZnFe_2O_4$ peaks at 29.9°, 35.2°, 42.8°, 52.9°, 56.5° and 62.1° are attributed to the (220), (311), (400), (422), (511), and (440) crystal planes of spinel $ZnFe_2O_4$ (JCPDS:79-1150), respectively [68]. The typical diffraction peaks of BiOBr centered at 2θ values of 10.9°, 25.2°, 31.7°, 32.2°, 46.2° and 57.2° are indexed to (001), (101), (102), (110), (200), and (212) crystalline planes of tetragonal BiOBr (JCPDS:78-0438), respectively [69]. The above results indicate that GO, $ZnFe_2O_4$ nanocrystals and BiOBr nanocrystals are pure phases with good crystallinity. In the XRD pattern of BOB/ZFO NCs, all characteristic peaks of BiOBr nanocrystals and some diffraction peaks (35.2° and 62.1°) of $ZnFe_2O_4$ nanocrystals can be observed and the crystallinity of $ZnFe_2O_4$ nanocrystals is weaker than that of BiOBr nanocrystals, which may be due to the fact that the mass of $ZnFe_2O_4$ nanocrystals is less than that of BiOBr nanocrystals [70]. After adding GO to BOB/ZFO NCs, due to the limited amount of GO, BOB/ZFO-GO(2) can only exhibit peaks similar to BOB/ZFO NCs and no characteristic peaks of GO are found [71]. Subsequently, to prove GO presence, we analyzed and compared the XRD patterns of BOB/ZFO-GO NCs containing GO additions (BOB/ZFO-GO(1), BOB/ZFO-GO(2), BOB/ZFO-GO(3)), as illustrated in Fig. 1(b). Enlarged XRD spectra of (102) and (110) planes of BiOBr nanocrystals show that the XRD peaks of BOB/ZFO-GO NCs exhibit an obvious shift towards higher angle compared to those of BOB/ZFO NCs and this phenomenon is more obvious with the increase of GO amount. The (102) and (110) crystal faces of BiOBr nanocrystals of BOB/ZFO NCs and BOB/ZFO-GO(3) move from 31.56° and 32.14° to 31.75° and 32.31°, respectively, which indirectly proves the existence of GO [72]. Raman spectroscopy was used to further prove the existence of GO. Fig. 1(c) presents the Raman signals from pure GO and BOB/ZFO-GO(2). It is well known that the most prominent Raman characteristics of GO are the D (disordered carbon) and G (graphite carbon) bands, located at about 1350 and 1587 $cm^{-1}$, correspondingly [73]. Two representative peaks of GO are visible in Raman spectrum of BOB/ZFO-GO(2), indicating the presence of GO in the composite system. Compared with pure GO, the slight shift of the Raman peak position of BOB/ZFO-GO(2) is attributed to the interaction between GO and BOB/ZFO [74]. In addition, it is reasonable that the Raman band intensities of BOB/ZFO-GO(2) are weaker than those of pure GO, given that the GO content of BOB/ZFO-GO(2) is lower than that of pure GO [75]. FT-IR spectroscopy was employed to observe the functional groups of the prepared samples. FTIR spectra of GO, $ZnFe_2O_4$ nanocrystals, BiOBr nanocrystals, BOB/ZFO NCs and BOB/ZFO-GO(2) are presented in Fig. 1(d). Four distinctive peaks of GO appear at 1051, 1225, 1407 and 1603 $cm^{-1}$, resulting from the stretching vibration of C—O, C—O—C, C=C and C=O groups, respectively [76]. As for pure $ZnFe_2O_4$ nanocrystals, the characteristic infrared peaks at 440 and 550 $cm^{-1}$ correlate with the vibrations of the Fe-O and Zn-O of spinel $ZnFe_2O_4$, respectively [77]. The FT-IR peak of pure BiOBr nanocrystals is located at 507 $cm^{-1}$, which belongs to the Bi-O bond symmetric streching vibration [78]. In comparison with pure BiOBr nanocrystals, a weak absorption at 537 $cm^{-1}$ is observed in BOB/ZFO NCs, which is derived from $ZnFe_2O_4$ nanocrystals in the sample. This result demonstrates that $ZnFe_2O_4$ nanocrystals are successfully compounded on the surface of BiOBr nanocrystals. As for the FT-IR spectrum of BOB/ZFO-GO(2), the characteristic peaks of both of GO and BOB/ZFO NCs are retained, which can further prove the successful synthesis of BOB/ZFO-GO NCs. Furthermore, the peaks within 3000–3500 $cm^{-1}$ are observed for all samples, which are assigned to the streching vibrations of adsorbed molecular water or O—H groups.

The microscopic morphology of the synthetic samples was analyzed by means of SEM and TEM. From Fig. S1(a), it is clear that GO exhibits
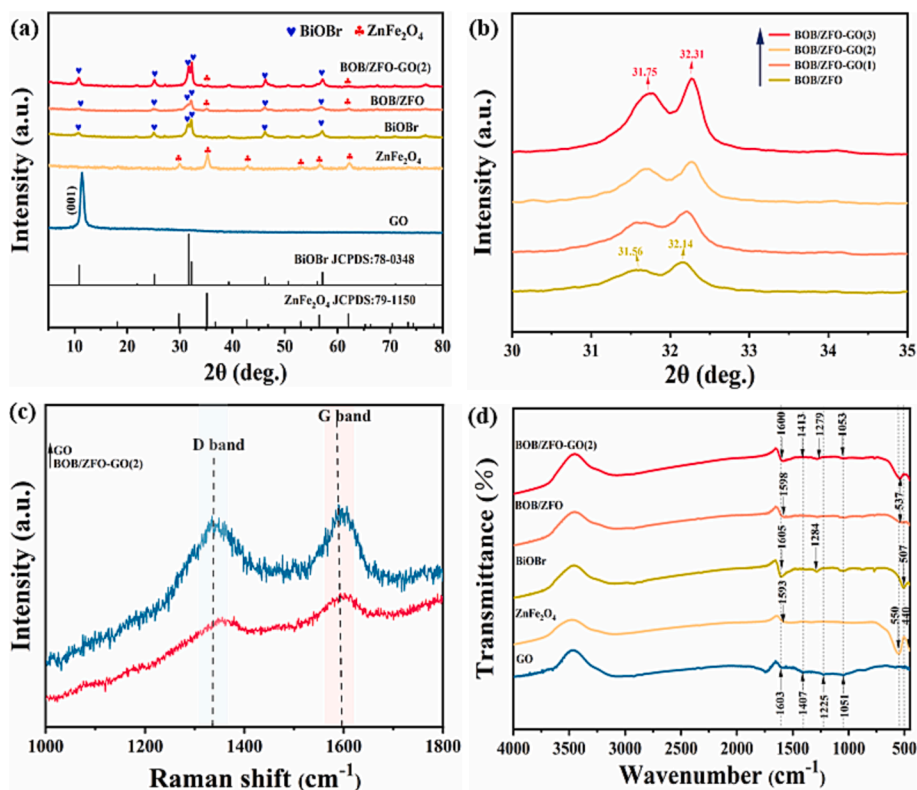


**Fig. 1.** (a) XRD spectra of GO, $ZnFe_2O_4$ nanocrystals, BiOBr nanocrystals, BOB/ZFO NCs and BOB/ZFO-GO(2); (b) enlarged XRD patterns of BOB/ZFO NCs, BOB/ZFO-GO(1), BOB/ZFO-GO(2) and BOB/ZFO-GO(3) in the 2θ range of 30-35°; (c) Raman spectra of GO and BOB/ZFO-GO(2) and (d) FTIR spectra of GO, $ZnFe_2O_4$ nanocrystals, BiOBr nanocrystals, BOB/ZFO NCs and BOB/ZFO-GO(2).

2D layered structure with a folded surface and irregular edges [79]. Fig. S1(b) shows that ZnFe$_2$O$_4$ nanocrystals present a flower ball-like nanostructure with curly petals, with an average size of around 0.8 ~ 1 μm and good dispersion. The prepared BiOBr nanocrystals are homogeneous spherical structures with a diameter ranging from 4.0 ~ 5.0 μm, which is depicted in Fig. S1(c). The SEM image of BOB/ZFO NCs in Fig. S1(d) indicates that ZnFe$_2$O$_4$ nanocrystals are randomly anchored on the surfaces of BiOBr nanocrystals. The SEM and TEM results of BOB/ZFO-GO(2) are given in Fig. 2(a)-(b). It can be noticed that BiOBr nanocrystals and ZnFe$_2$O$_4$ nanocrystals are obviously present on the surface of the GO surfaces to form BOB/ZFO-GO nanostructures with close contact interfaces. This structure can effectively accelerate the separation and transport of photogenerated carriers between BiOBr nanocrystals and ZnFe$_2$O$_4$ nanocrystals in the photocatalytic process. In addition, the high-resolution TEM (HRTEM) image of BOB/ZFO-GO(2) in Fig. 2(c) demonstrates the facet spacing of 0.235 nm and 0.167 nm matches with (1 0 1) crystallographic facets of the BiOBr nanocrystals and (2 2 0) crystallographic facets of the ZnFe$_2$O$_4$ nanocrystals. The elemental mapping images corresponding to Fig. 2(a) show a uniform distribution of Bi, Br, Fe, Zn, O and C elements in the sample, also suggesting the successful construction of BOB/ZFO-GO ternary NCs. Furthermore, the EDS results of BOB/ZFO-GO(1), BOB/ZFO-GO(2) and BOB/ZFO-GO(3) are exhibited in Fig. S2, which shows that the proportion of C atoms increases with the increase of the amount of GO.

The surface elemental components and chemical states of the prepared BOB/ZFO-GO(2) were detected by XPS spectroscopy. The C 1s peak at 284.8 eV was used as a reference for charge correction. As presented in Fig. S3, the peaks of six elements, including Bi, Br, O, Zn, Fe and C, are clearly visible in the XPS full spectrum. The Bi 4f XPS spectrum for BOB/ZFO-GO(2) in Fig. 3(a) displays that the peaks at 159.5 eV and 164.9 eV correspond to Bi 4f$_{7/2}$ and Bi 4f$_{5/2}$, respectively, which are consistent with the orbitals of Bi$^{3+}$ in BiOBr [80]. Concerning Br 3d spectrum in Fig. 3(b), two peaks at 68.6 eV and 69.6 eV are assigned to Br 3d$_{5/2}$ and Br 3d$_{3/2}$, respectively, confirming the presence of Br ions [81]. The XPS spectrum of O 1s in Fig. 3(c) can be fitted into three characteristic peaks. The first peak at 530.4 eV is in agreement with the surface lattice oxygen in the Bi-O, Fe-O and Zn-O. The second peak at 531.8 eV is attributed to the metal-hydroxyl groups (Zn-OH, Fe-OH and Bi-OH) and carbon-hydroxyl groups (C-OH). The last peak at 533.2 eV is owing to surface-adsorbed oxygen [82]. For the case of Zn 2p spectrum (Fig. 3(d)), two main signals are located in 1021.5 eV and 1044.6 eV, corresponding to Zn 2p$_{3/2}$ and Zn 2p$_{5/2}$, respectively, which confirms the presence of Zn$^{2+}$ oxidation state in the structure of BOB/ZFO-GO(2) sample. In Fig. 3(e), two peaks with binding energies of 711.6 eV and 725.3 eV are associated with Fe 2p$_{3/2}$ and Fe 2p$_{1/2}$, respectively, which implies that Fe element exists in the form of Fe$^{3+}$ in BOB/ZFO-GO(2) sample [33]. From the C 1s XPS spectrum in Fig. 3(f), it is evident that the doublet signs located at 285.1 eV and 288.4 eV belong to sp$^2$ C—C bond and C—O bond, respectively [83]. In summary, the above XPS results indicate the successful preparation of BiOBr/ZnFe$_2$O$_4$-GO NCs.

## 3.2. Physical, optical and photoelectrochemical properties

As we all know, a larger surface area can provide larger contact area, which can offer a greater number of reactive sites for the photocatalytic process and thus facilitate the improvement of photocatalytic efficiency. The BET specific areas of the four photocatalysts were tested, as presented in Fig. 4(a). N$_2$ adsorption–desorption isotherms of BiOBr nanocrystals, ZnFe$_2$O$_4$ nanocrystals, BOB/ZFO NCs and BOB/ZFO-GO (2) belong to the typical type IV isotherm with Type H3 hysteresis loops, which implies that these four samples have mesoporous structures and this will be beneficial to the adsorption of TC. The specific surface areas of BiOBr nanocrystals, ZnFe$_2$O$_4$ nanocrystals, BOB/ZFO NCs and BOB/ZFO-GO(2) are calculated to be 17.04, 34.19, 37.79 and 42.47 m$^2$/g, respectively. The results show that the specific area of BOB/ZFO NCs significantly increases compared with BiOBr and ZnFe$_2$O$_4$ nanocrystals. The specific area of BOB/ZFO-GO(2) further increases, suggesting that the introduction of GO can decrease the aggregation of BOB/ZFO NCs and thus lead to more exposed BOB/ZFO NCs. In addition, the pore size distribution and the pore volume of the four samples were determined using Barrett-Joyner-Halenda (BJH) method. Fig. 4(a) indicates the pore sizes are mainly distributed between 2 and 40 nm. The smaller pores may originate from the ZnFe$_2$O$_4$ and BiOBr nanocrystals, while the formation of larger pores may be related to the addition of GO. The above results show that BOB/ZFO-GO(2) has the highest porosity and specific surface area, which may supply a greater number of reactive sites and thereby achieve higher photocatalytic performance. The specific area, the pore size and the pore volume of the four photocatalysts are given in Table 1.

The light absorption capacity of samples was investigated using UV–Vis DRS. As exhibited by Fig. 4(b), pure BiOBr nanocrystals show remarkable absorption in the visible region near the absorption edge at around 430 nm. In comparison, ZnFe$_2$O$_4$ nanocrystals exhibit a wide absorption capacity and cover the entire UV–Vis light range. The combination of BiOBr nanocrystals with ZnFe$_2$O$_4$ nanocrystals results in a significant increase in the optical absorption properties of pure BiOBr nanocrystals, especially in the visible region (wavelength > 400 nm). Moreover, the visible absorption efficiency of BOB/ZFO-GO(2) has been further improved compared to BOB/ZFO NCs due to the introduction of
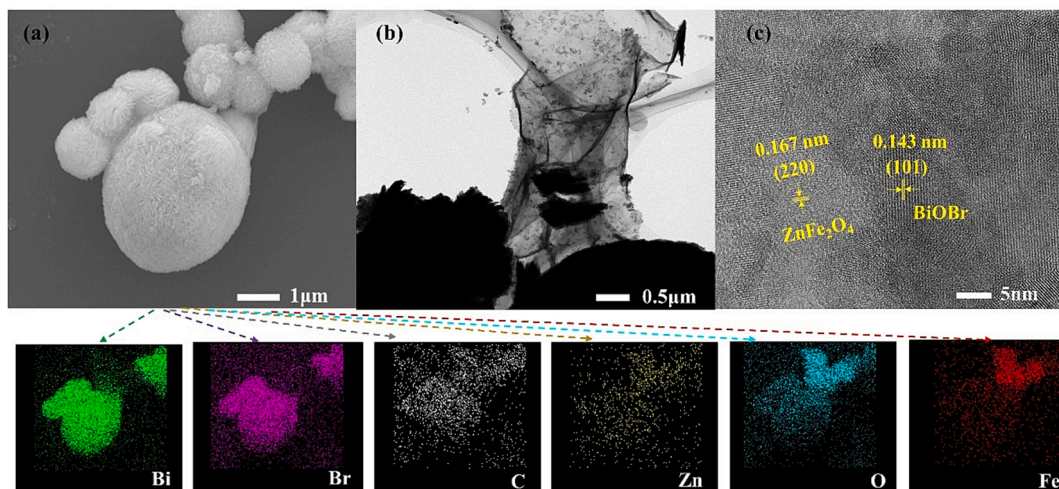


**Fig. 2.** (a) SEM, (b) TEM, (c) HRTEM and (d) elements mapping images of BOB/ZFO-GO(2).
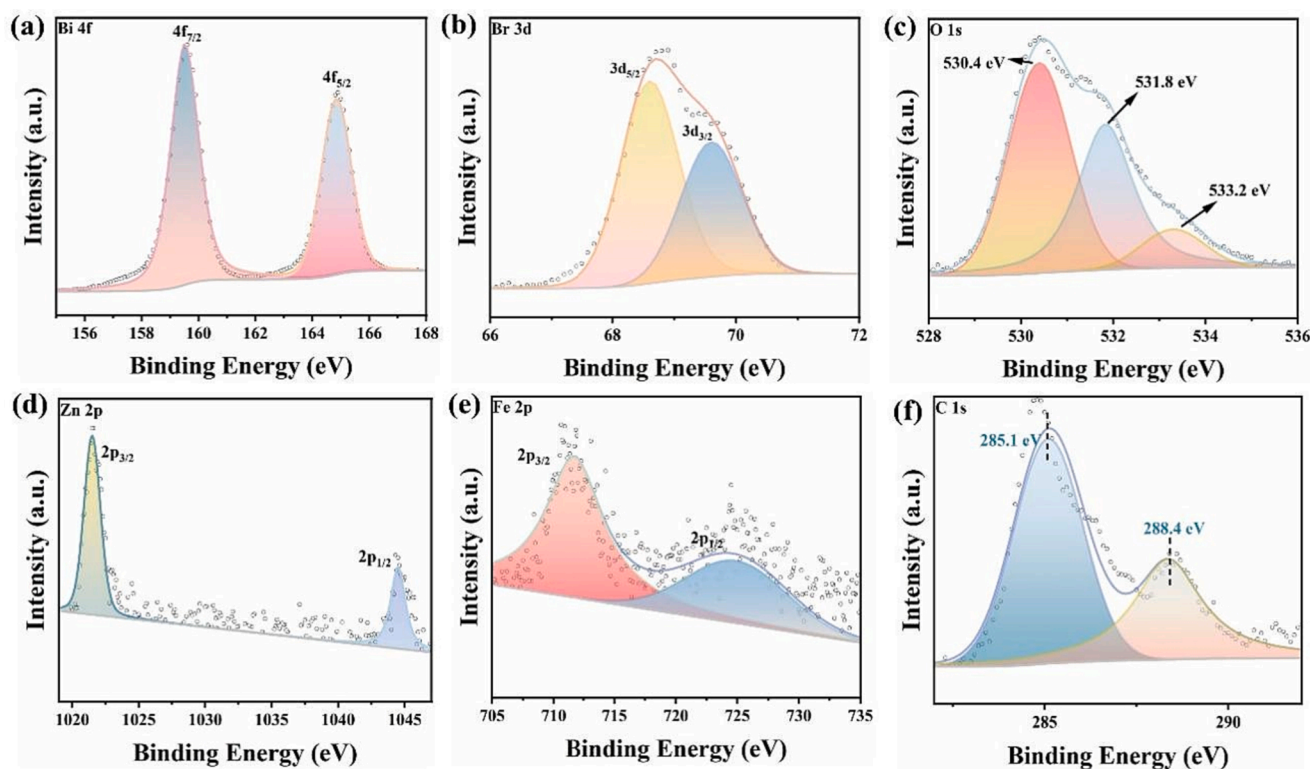
**Fig. 3.** High-resolution XPS spectrum corresponding to (a) Bi 4f, (b) Br 3d, (c) O 1s, (d) Zn 2p, (e) Fe 2p and (f) C 1s of BOB/ZFO-GO(2).

GO. Therefore, UV–Vis DRS analysis strongly verifies the formation of S-scheme heterojunction. Moreover, since BiOBr nanocrystals, ZnFe$_2$O$_4$ nanocrystals and their composites are regarded as indirect semiconductors, the energy band energy ($E_g$) of the photocatalyst was computed using the Kubelka-Munk formula in conjunction with UV–Vis DRS findings, as shown in the following equation:

$$(\alpha h v)^{1/2} = A\big(h v \, - \, E_g\big) \tag{1}$$

In which, $\alpha$, $h$, $\nu$, $A$ and $E_g$ are the absorption factor, Planck's constant, vibration frequency, proportion and bandgap energy, respectively [84]. As seen in the inset of Fig. 4**(b)**, the $E_g$ is determined by the intercept of the tangent line of $(\alpha h v)^{1/2}$ with the $h v$ curve. Accordingly, the bandgap energies of pure BiOBr nanocrystals and ZnFe$_2$O$_4$ nanocrystals are estimated to be about 2.6 and 1.57 eV, respectively. The conduction band potential ($E_{CB}$) and valence band potential ($E_{VB}$) of a semiconductor can be calculated by the following formula:

$$E_{VB} = X - E_e \, + \, 0.5E_g \tag{2}$$

$$E_{CB} = E_{VB} \, - \, E_g \tag{3}$$

where $X$ and $E_e$ are the geometric means of the Pearson absolute electronegativity and the energy of the free electron on the hydrogen scale (4.5 eV), respectively. And the absolute electronegativity of the semiconductor can be computed as follows [85]:

$$X(A_m B_n C_l) = {}^{(m+n+l)}\sqrt{X_{Am} X_{Bn} X_{Cl}} \tag{4}$$

The absolute electronegativities of Bi, O, Br, Fe and Zn are 4.69, 7.54, 7.59, 4.06 and 4.45 eV, correspond to X(BiOBr) and X(ZnFe$_2$O$_4$) of 6.45 and 5.86 eV, respectively. From **Eq. (2)-(3)**, the $E_{VB}$ of pure BiOBr nanocrystals and pure ZnFe$_2$O$_4$ nanocrystals is 3.25 and 2.15 eV, and the $E_{CB}$ is 0.65 and 0.58 eV, respectively. The result shows that pure BiOBr nanocrystals and pure ZnFe$_2$O$_4$ nanocrystals have interleaved energy band structures, which match well with the band potential of S-scheme heterojunction. Compared to pure BiOBr nanocrystals and pure ZnFe$_2$O$_4$

nanocrystals, the band gaps of BOB/ZFO NCs and BOB/ZFO-GO(2) are reduced to about 1.47 and 1.24 eV, respectively. These results can be attributed to the construction of a dual semiconductor S-scheme heterojunction and the improved interfacial interaction between some unpaired π-electrons of the conjugated carbon atom and the free electrons on the semiconductor surface owing to the addition of GO, respectively [86].

The PL spectrum was used to analyze photogenerated carrier separation and transfer ability of prepared samples [87]. In general, lower PL intensity indicates higher photoexcited electron-hole pairs separation efficiency. The PL spectra of BiOBr nanocrystals, ZnFe$_2$O$_4$ nanocrystals, BOB/ZFO NCs, BOB/ZFO-GO(1), BOB/ZFO-GO(2) and BOB/ZFO-GO(3) are compared in Fig. 4**(c)**. It can be found that the PL peak intensity of BOB/ZFO NCs is lower than that of pure BiOBr nanocrystals and pure ZnFe$_2$O$_4$ nanocrystals, which proves that the construction of S-scheme heterojunction effectively suppresses the recombination of photogenerated electron-hole pairs. In addition, the PL peak intensity of all BOB/ZFO-GO NCs is lower than that of BOB/ZFO NCs, indicating that the electron-hole pairs migration is further enhanced after the combination of BOB/ZFO NCs and GO. GO can greatly suppress carrier recombination and thus enhance photocatalytic activity. The PL emission intensity is also related to the GO content, and the lowest PL emission intensity is observed in the BOB/ZFO-GO(2). Excess GO in the BOB/ZFO-GO(3) leads to an increase in the peak intensity, which may be attributed to the aggregation of GO and the resultant inhibitory effect on charge separation [72].

Photoelectrochemical experiments provide further information on the charge generation and transfer properties of as-prepared samples [88]. The transient photocurrent response of the six samples is shown in Fig. 4**(d)**. All samples have reproducible and fast photocurrent response when light is irradiated to the test system, and the photocurrent intensity rapidly decreases to zero once the light excitation stops. The photocurrent density of BOB/ZFO NCs is stronger than that of pure BiOBr nanocrystals and pure ZnFe$_2$O$_4$ nanocrystals, which can be attributed to the enhanced internal charge migration of the S-scheme
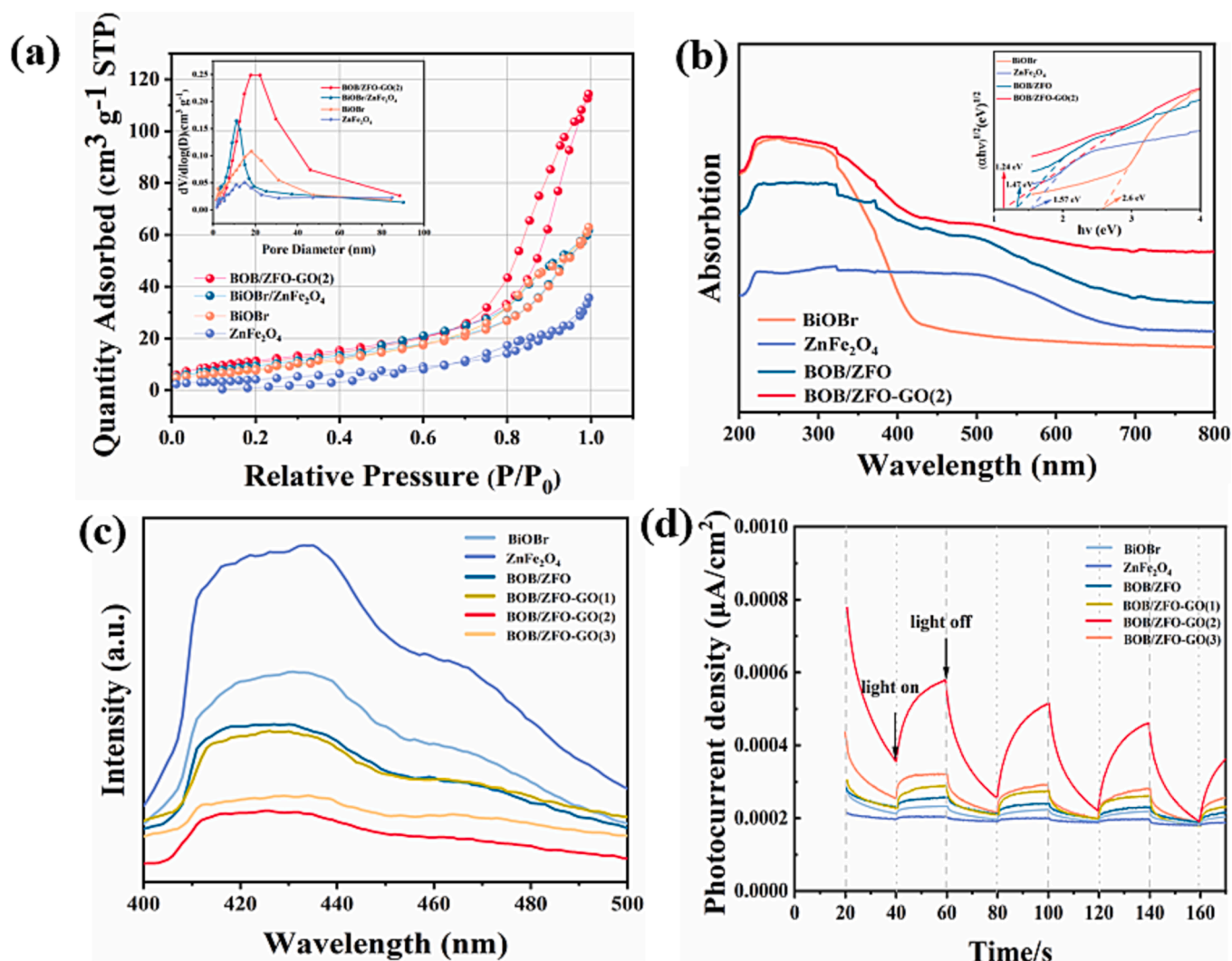
**Fig. 4.** (a) $N_2$ adsorption–desorption isotherm and (inset) pore distribution curve and (b) UV–Vis DRS and (inset) plot of $(\alpha h\nu)^{1/2}$ versus $h\nu$ of BiOBr nanocrystals, $ZnFe_2O_4$ nanocrystals, BOB/ZFO NCs and BOB/ZFO-GO(2); (c) PL spectra and (d) photocurrent transient responses of BiOBr nanocrystals, $ZnFe_2O_4$ nanocrystals, BOB/ZFO NCs, BOB/ZFO-GO(1), BOB/ZFO-GO(2) and BOB/ZFO-GO(3), respectively.

**Table 1**
The pore structure parameters of BiOBr nanocrystals, $ZnFe_2O_4$ nanocrystals, BOB/ZFO NCs and BOB/ZFO-GO(2).

| Sample | $S_{BET}$ ($m^2/g$) | Pore size (nm) | Pore volume ($cm^3\ g^{-1}$) |
|---|---|---|---|
| BiOBr | 34.19 | 14.87 | 0.095 |
| $ZnFe_2O_4$ | 17.04 | 18.02 | 0.055 |
| BOB/ZFO | 37.79 | 11.03 | 0.097 |
| BOB/ZFO-GO(2) | 42.47 | 22.12 | 0.176 |

heterojunction network formed by the two semiconductors. Meanwhile, BOB/ZFO-GO has a higher photocurrent response than BOB/ZFO NCs, which indicates that GO is a conductive medium and can facilitate the transfer of electrons in optical radiation. With the increase of GO content, the photocurrent density of BOB/ZFO-GO NCs increases and then decreases, and the photocurrent density of BOB/ZFO-GO(2) is the largest, which is consistent with the results of PL spectra.

### 3.3. Photocatalytic performance, magnetic properties and stability evaluation

The photocatalytic capability of BOB/ZFO-GO(2) was investigated through degradation of TC exposed to simulated sunlight irradiation.

UV–Vis absorption spectra of BOB/ZFO-GO(2) for the degradation of TC at different reaction times are illustrated in Fig. 5(a). The characteristic peak of TC at ~ 360 nm decays rapidly when increasing time of the photocatalytic reaction and eventually vanishes, which indicates that BOB/ZFO-GO(2) can completely degrade TC within 80 min when exposed to simulated solar irradiation. A sequence of TC degradation tests were performed to evaluate the photocatalytic capability of the different samples, and the TC solution with no addition of any photocatalyst was used as a blank reference. TC solution containing photocatalyst was allowed to stand for 40 min in a dark room to achieve adsorption equilibrium. As exhibited in Fig. 5(b), the adsorption capacity of the composite materials including BOB/ZFO NCs and BOB/ZFO-GO NCs (BOB/ZFO-GO(1), BOB/ZFO-GO(2), BOB/ZFO-GO(3)) is significantly greater than that of the monomeric material (BiOBr and $ZnFe_2O_4$ nanocrystals). This outcome can be explained by the rise in specific surface area, which can be observed in BET test. Then, after 80 min of light exposure, the removal effect of TC solution by different as-prepared photocatalysts was also investigated. There is no significant change in the blank control, demonstrating the high stability of TC. All of the composites have better TC solution degradation activity than the individual BiOBr and $ZnFe_2O_4$ nanocrystals, which can be testified by the corresponding linear correlation between $ln(C_t/C_0)$ in Fig. 5(c). The UV–Vis absorption spectra of TC catalyzed by BiOBr and $ZnFe_2O_4$
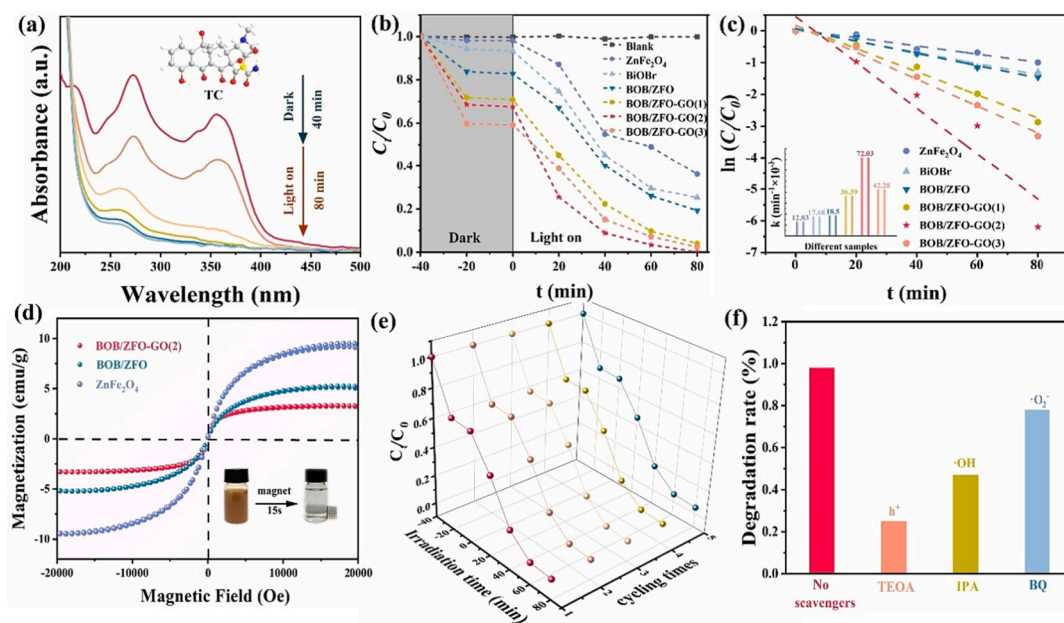
**Fig. 5.** (a) UV–Vis absorption spectra of TC catalyzed by BOB/ZFO-GO(2) under simulated sunlight conditions; (b) $C_t/C_0$ versus reaction time and (c) corresponding first-order kinetic for TC catalyzed by BiOBr nanocrystals, ZnFe$_2$O$_4$ nanocrystals, BOB/ZFO NCs and BOB/ZFO-GO NCs (BOB/ZFO-GO(1), BOB/ZFO-GO(2) and BOB/ZFO-GO(3)); (d) *M−H* loops of ZnFe$_2$O$_4$ nanocrystals, BOB/ZFO NCs and BOB/ZFO-GO(2) (The inset is photograph of BOB/ZFO-GO(2) dispersed in deionized water before and after separation by a magnet); (e) cycling tests of BOB/ZFO-GO(2) for TC degradation at same experimental situation and (f) the degradation rate of TC including different scavengers in the attendance of BOB/ZFO-GO(2) after 80 min irradiation.

nanocrystals under simulated daylight conditions are shown in Fig. S4. From highest to lowest, the values of kinetic rate constant are as follows: BOB/ZFO-GO(2) > BOB/ZFO-GO(1) > BOB/ZFO-GO(3) > BOB/ZFO > BiOBr > ZnFe$_2$O$_4$. BOB/ZFO-GO(2) has the greatest reaction rate constant (72.03 min$^{-1}$ × 10$^{-3}$) and TC degradation efficiency when compared with other photocatalysts.

The magnetic properties of the photocatalysts were investigated at room temperature using VSM. Magnetic hysteresis (*M−H*) loops of ZnFe$_2$O$_4$ nanocrystals, BOB/ZFO NCs and BOB/ZFO-GO(2) are presented in Fig. 5(d), which possess saturation magnetization (*Ms*) value of 9.43, 5.18 and 3.29 emu·g$^{-1}$, respectively. Even though the addition of BiOBr and GO reduces the Ms value, BOB/ZFO-GO(2) still exhibits a good magnetic response and it can be effortlessly separated from the suspension within 15 s when exposed to an additional magnetic field, as can be observed from the inserted portion of Fig. 5(d). The great magnetic response performance provides BOB/ZFO-GO(2) with the ability to be recycled. The cyclic degradation experiments of TC were performed under light to further assess the reusability and stability of BOB/ZFO-GO(2). Fig. 5(e) demonstrates that the TC photocatalytic efficiency does not decrease obviously during five cycle processes, indicating that the BOB/ZFO-GO(2) has a high degree of reusability. Moreover, the BOB/ZFO-GO(2) after the cycling experiments was characterized using XRD and XPS to further confirm the stability of the prepared material [89]. As shown in Fig. S5(a), the characteristic peaks of the used BOB/ZFO-GO(2) are almost identical to those of the original BOB/ZFO-GO(2), indicating that the crystal structure BOB/ZFO-GO(2) is stable. In addition, there are no appreciable differences in the peak positions and intensities of the Bi 4f, Br 3d, C 1s, O 1s, Zn 2p, and Fe 2p spectra, further demonstrating the chemical stability of the prepared BOB/ZFO-GO(2) (Fig. S5(b)-(h)). Based on the above results, it can be inferred that BOB/ZFO-GO(2) has high physical and chemical stability and can be considered as a potential candidate for degradation and detection of TC. In situ free radical trapping experiments were carried out with the aim of further identifying the active species contributing to the degradation of TC. Herein, each trapping agent employed in this experiment is kept at a concentration of 5 mM. TEOA, IPA and BQ are used as capture agents to trap h$^+$, ·OH and·O$^{2-}$, respectively. As displayed in Fig. 5(f), the degradation rate

of TC can reach 98% without the addition of scavenger. It is clear that the three active species including h$^+$, ·OH and ·O$^{2-}$ are involved in the photocatalytic degradation of TC because TEOA, IPA and BQ more or less hinder the photocatalytic activity of BOB/ZFO-GO(2) and cause a decrease in the degradation rate of TC. In particular, the catalytic capacity of BOB/ZFO-GO(2) is considerably reduced when TEOA is added to the photocatalytic process, and the removal rate of TC drops from 98% to 22%. This implies that h$^+$ is the predominant reactive species for triggering TC degradation. In contrast, after the addition of BQ to the reaction system, the degradation efficiency decreases slightly, indicating that ·O$^{2-}$ may not be a crucial factor in the TC degradation reaction. Additionally, when IPA is introduced into the photocatalytic system, the reaction rate is between TEOA and BQ, which suggests that ·OH makes a relatively significant contribution to the degradation of TC. Based on the above analysis, we believe that all three reactive radicals are engaged in the degradation of TC, with h$^+$ and ·OH being particularly important in the photocatalytic process.

### 3.4. Photocatalytic degradation performance evaluation under assistance of photothermal effect

Notably, the photothermal effect acts as an extraordinary factor in enhancing photocatalytic performance of photocatalysts. For examining the photothermal performance of the photocatalysts, 1 g of BOB/ZFO NCs, BOB/ZFO-GO(1), BOB/ZFO-GO(2) and BOB/ZFO-GO(3) was dispersed into 100 mL of deionized water, respectively. The surface temperature changes upon their exposure to 5 min of 808 nm laser irradiation were recorded using a thermal imaging camera, and the deionized water was taken as the blank control. As illustrated in Fig. 6 (a), the BOB/ZFO NCs have no discernible temperature rise, which means that the photothermal effect of BiOBr nanocrystals and ZnFe$_2$O$_4$ nanocrystals can be almost negligible. Following the introduction of GO, the temperature of BOB/ZFO-GO(1), BOB/ZFO-GO(2) and BOB/ZFO-GO(3) gradually rises as irradiation time is prolonged, and the color displayed in the infrared thermal image gradually changes to red, among which the increase in temperature of BOB/ZFO-GO(3) is the fastest. The corresponding photothermal temperature curves are presented in Fig. 6
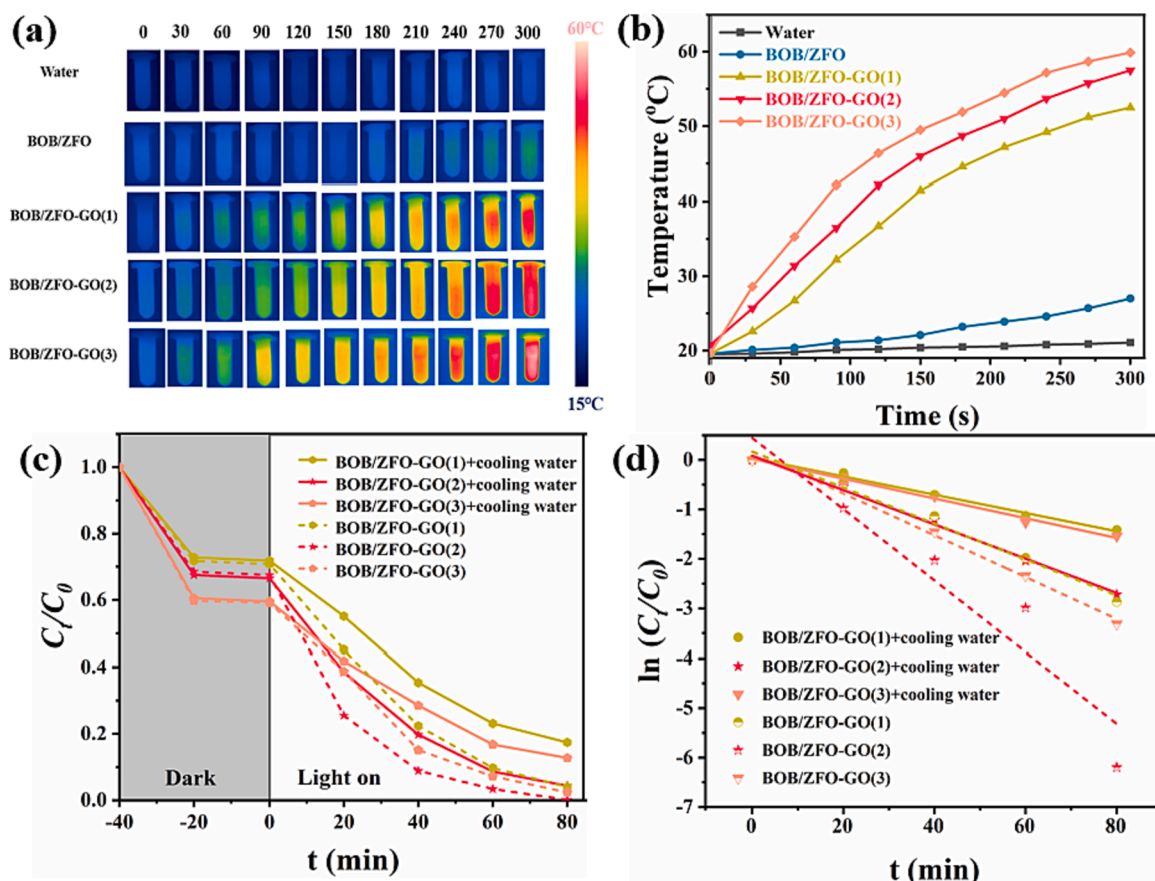
**Fig. 6.** (a) Infrared thermal images of BOB/ZFO NCs, BOB/ZFO-GO(1), BOB/ZFO-GO(2) and BOB/ZFO-GO(3) under 808 nm laser (1.5 W cm$^{-2}$) by 300 s and (b) corresponding photothermal temperature curves; (c) $C_t/C_0$ versus reaction time for TC catalyzed by BOB/ZFO-GO NCs (BOB/ZFO-GO(1), BOB/ZFO-GO(2) and BOB/ZFO-GO(3)) before and after the addition of cooling water and (d) corresponding first-order kinetic curves.

**(b)**. After 5 min of irradiation with 808 nm laser, the temperature of BOB/ZFO NCs only increases by 8 °C. In contrast, the introduction of GO can result in a significant temperature rise. And the more GO is added, the more obvious this phenomenon will be. The temperature of BOB/ZFO-GO(1), BOB/ZFO-GO(2) and BOB/ZFO-GO(3) has risen by 34.5, 38.8 and 41.9 °C, respectively. To investigate the effect of the photothermal characteristics of photocatalysts on photocatalytic reactions, the degradation efficiency of BOB/ZFO-GO(1), BOB/ZFO-GO(2) and BOB/ZFO-GO(3) for TC was tested and compared with and without the circulation of cooling water. Fig. 6**(c)** displays that the degradation efficiency of BOB/ZFO-GO NCs for TC is significantly reduced under the action of cooling water. The corresponding kinetic constants of BOB/ZFO-GO(1), BOB/ZFO-GO(2) and BOB/ZFO-GO(3) decrease from 0.036, 0.072 and 0.042 min$^{-1}$ to 0.018, 0.034 and 0.020 min$^{-1}$, respectively (Fig. 6**(d)**). In addition to serving as a carrier transport medium in the heterojunction to enhance the photocatalytic activity of the photocatalyst, the introduction of GO in BOB/ZFO NCs aids in speeding up the degradation of TC through its photothermal effect. By converting NIR radiation energy into thermal energy, GO raises the temperature of the photocatalytic system, which improves charge separation and intensifies molecular collisions, and strongly promotes carrier transfer [90]. As the carrier mobility increases, the BOB/ZFO-GO NCs maintain an excellent photothermal conversion effect, thereby achieving better TC removal efficiency. In conclusion, the perfect combination of the GO with the high photothermal effect and the dual semiconductor heterostructure greatly improves the degradation efficiency of BOB/ZFO-GO NCs for TC.

### 3.5. Mechanism analysis of photocatalytic system

According to the aforementioned experiment outcomes, two potential transfer mechanisms of photogenerated charge carriers including conventional type II and S-scheme photocatalytic mechanisms were proposed, which are shown in Fig. 7. In the type II heterojunction, both BiOBr nanocrystals and ZnFe$_2$O$_4$ nanocrystals can be activated by visible light to form e$^-$-h$^+$ pairs. The photogenerated e$^-$ in the CB of ZnFe$_2$O$_4$ nanocrystals can be transferred to BiOBr nanocrystals because they have a lower negative CB position than ZnFe$_2$O$_4$ nanocrystals. However, the CB potential of BiOBr (0.65 eV) is higher than O$_2$/·O$^{2-}$ (-0.33 eV vs normal hydrogen electrode (NHE)), suggesting that the O$_2$ cannot be reduced to ·O$^{2-}$. Fortunately, the GO with high conductivity can facilitate the transfer of e$^-$, so the e$^-$ accumulated on the CB of BiOBr nanocrystals may be easily transferred to the surface of GO and then reduce the O$_2$ trapped in the solution to ·O$^{2-}$. The migration direction of photogenerated h$^+$ is opposite to that of photogenerated e$^-$ due to the lower positive VB position of ZnFe$_2$O$_4$ nanocrystals compared to BiOBr nanocrystals. Given that the VB potential (2.15 eV) of ZnFe$_2$O$_4$ nanocrystals is lower than that of ·OH/H$_2$O (2.72 eV vs NHE) and ·OH/OH$^-$ (2.3 eV vs NHE), the photogenerated h$^+$ accumulated on the VB of ZnFe$_2$O$_4$ nanocrystals cannot oxidize the H$_2$O and OH$^-$ to ·OH. This is inconsistent with the results of the above free radical scavenging experiments, because ·OH is the major active species in the TC degradation process. Therefore, the S-scheme photocatalytic mechanism seems to be more convincing. When the BOB/ZFO-GO S-scheme system is exposed to visible light, the photogenerated e$^-$ migrates from the VB of BiOBr nanocrystals to CB. Meanwhile, induced by the built-in electric field, it recombines with the photogenerated h$^+$ at the VB of ZnFe$_2$O$_4$
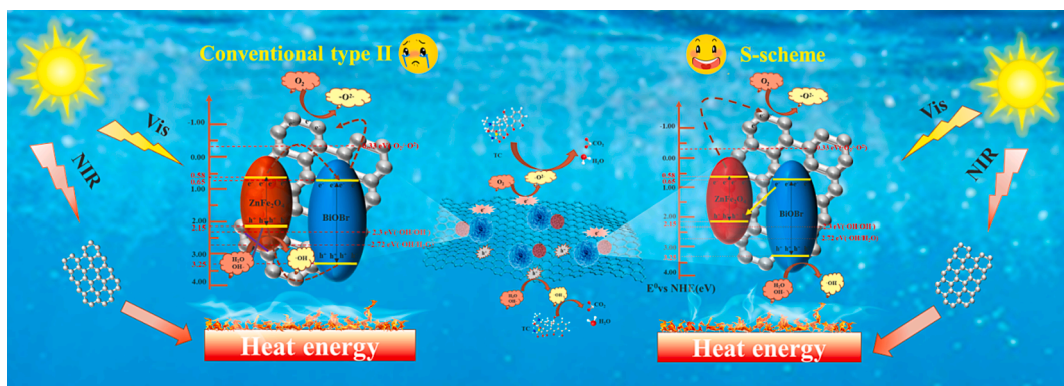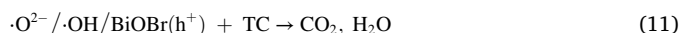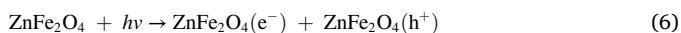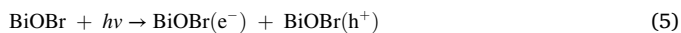
**Fig. 7.** Schematic illustration of possible charge migration and photocatalytic mechanisms from the degradation of TC by BOB/ZFO-GO NCs.

nanocrystals through the intermediate transport medium GO. Correspondingly, the photogenerated $h^+$ in the VB of BiOBr nanocrystals and the photogenerated $e^-$ in the CB of $ZnFe_2O_4$ nanocrystals are retained. The VB edge of BiOBr nanocrystals is enough positive potential (3.25 eV) to oxidize $H_2O$ and $OH^-$ to form $\cdot OH$, which is consistent with the results of free radical trapping experiments. Therefore, the prepared BOB/ZFO-GO NCs should be S-scheme heterojunction instead of the conventional type II heterojunction. As for the GO in BOB/ZFO-GO NCs, on the one hand, it acts as a charge transfer bridge to improve the separation efficiency of $e^-$-$h^+$ pairs on the dual semiconductors. On the other hand, the elevated temperature due to its photothermal effect can further accelerate the transfer of electrons. As a result, the photocatalytic performance of BOB/ZFO-GO NCs can be significantly improved because the radicals ($\cdot O^{2-}$, $h^+$ and $\cdot OH$) in the S-scheme photocatalytic system are engaged in the photocatalytic degradation process of TC. The detailed reactive processes are listed as follows:

$$BiOBr + hv \rightarrow BiOBr(e^-) + BiOBr(h^+) \tag{5}$$

$$ZnFe_2O_4 + hv \rightarrow ZnFe_2O_4(e^-) + ZnFe_2O_4(h^+) \tag{6}$$

$$BiOBr(e^-) + ZnFe_2O_4(h^+) \rightarrow hv \tag{7}$$

$$GO + ZnFe_2O_4(e^-) \rightarrow GO(e^-) \tag{8}$$

$$H_2O/OH^- + BiOBr(h^+) \rightarrow \cdot OH \tag{9}$$

$$O_2 + GO(e^-) \rightarrow \cdot O^{2-} \tag{10}$$

$$\cdot O^{2-}/\cdot OH/BiOBr(h^+) + TC \rightarrow CO_2, H_2O \tag{11}$$

### 3.6. Photothermal detection performance based on BOB/ZFO-GO(2)

While achieving effective photocatalytic degradation for TC, performing trace detection of TC is equally important. Given that BOB/ZFO-GO(2) has the optimal photocatalytic performance, it was chosen for the quantitative detection of concentration of TC by its photothermal signal generated during the photothermal detection process. The photothermal conversion performance of the BOB/ZFO-GO(2) was first assessed. In order to determine the photothermal conversion coefficient (η) of BOB/ZFO-GO(2), it was irradiated to an 808 nm laser continuously by 300 s and cooled down naturally by turning off the laser. η can be obtained from the following equation [51]:

$$\eta = \frac{hS(T_{max} - T_{surr}) - Q_{Dis}}{I(1 - 10^{-A_\lambda})} \tag{12}$$

Therein, $h$ and $S$ are the heat transfer coefficient and the surface area of the container, respectively. $I$ means the incident energy of the NIR laser with a value of 1.17 W (1.5 W $cm^{-2}$, spot diameter = 10 mm) and $A_\lambda$

represents the absorbance of the aqueous solution of BOB/ZFO-GO(2) at 808 nm, which is 0.057. $Q_{Dis}$ is so small as to be negligible. And $hS$ can be calculated by the following formula:

$$hS = \frac{\sum mC_p}{\tau_s} \tag{13}$$

where $m$ and $C_P$ are the mass of the solution (50 mg) and the specific heat capacity of the solvent water (4.2 J $g^{-1}$), respectively. The time constant $\tau_s$ can be determined by fitting the slope of the natural cooling time (300 ~ 600 s) versus -ln(θ). The dimensionless parameter θ is defined as follows:

$$\theta = \frac{T - T_{surr}}{T_{max} - T_{surr}} \tag{14}$$

$T$, $T_{surr}$ and $T_{max}$ represent the solution temperature at any given measurement time, the ambient temperature (20.8 °C) and the highest temperature after 300 s of irradiation (57.5 °C), respectively. From Fig. 8 (a), the slope value $\tau_s$ is 196.55 s, which leads to a calculated value of $hS$ = 0.00106 mW/ °C. By substituting the aforementioned parameters into equation (12), the η value of BOB/ZFO-GO(2) is calculated to be 27.2%. Despite the fact that BOB/ZFO NCs are made of non-noble metals, they exhibit a photothermal effect that is comparable to that of noble metals. Meanwhile, the photothermal stability of BOB/ZFO-GO(2) was also investigated. Fig. 8(b) demonstrates that maximum temperature of the solution containing BOB/ZFO-GO(2) is still comparatively stable after six laser on/off cycles. These results indicate that BOB/ZFO-GO(2) has high photothermal conversion efficiency and photothermal stability. In order to establish a photothermal detection platform for specific identification of targets, we prepared Apt-BOB/ZFO-GO(2) NCs by modifying the surface of BOB/ZFO-GO(2) with aptamers to achieve quantitative analysis of TC concentrations and the process is shown in Scheme 2. The absorption spectra before and after conjugating Apt to BOB/ZFO-GO(2) were compared. As illustrated in Fig. S6, after the Apt is modified, the supernatant produced by centrifuging BOB/ZFO-GO (2) has a significantly lower absorption peak at 260 nm than the supernatant obtained before the Apt is modified. Thus, it indicates that the Apt is successfully immobilized on the surfaces of BOB/ZFO-GO(2). Apt-modified BOB/ZFO-GO(2)-based photothermal sensor was utilized to detect the TC aqueous solutions with different concentrations. TC with different concentrations ($10^{-4}$, $10^{-3}$, $10^{-2}$, $10^{-1}$, 1, 10 and $10^2$ ng/mL) in combination with Apt-modified BOB/ZFO-GO(2) NCs were exposed to 808 nm laser, respectively. Temperature of all the solutions gradually increases with increasing irradiation time, until they reach a constant value after 300 s (Fig. 8(c)). As shown in Fig. 8(d), the temperature increase (ΔT) is linearly and quantitatively correlated with the logarithm of TC concentration. The squared correlation coefficient ($R_2$) value of the linear regression equation, ΔT = 3.45 logC + 20.92, is as high as 0.997. It can be concluded that the Apt-modified BOB/ZFO-GO
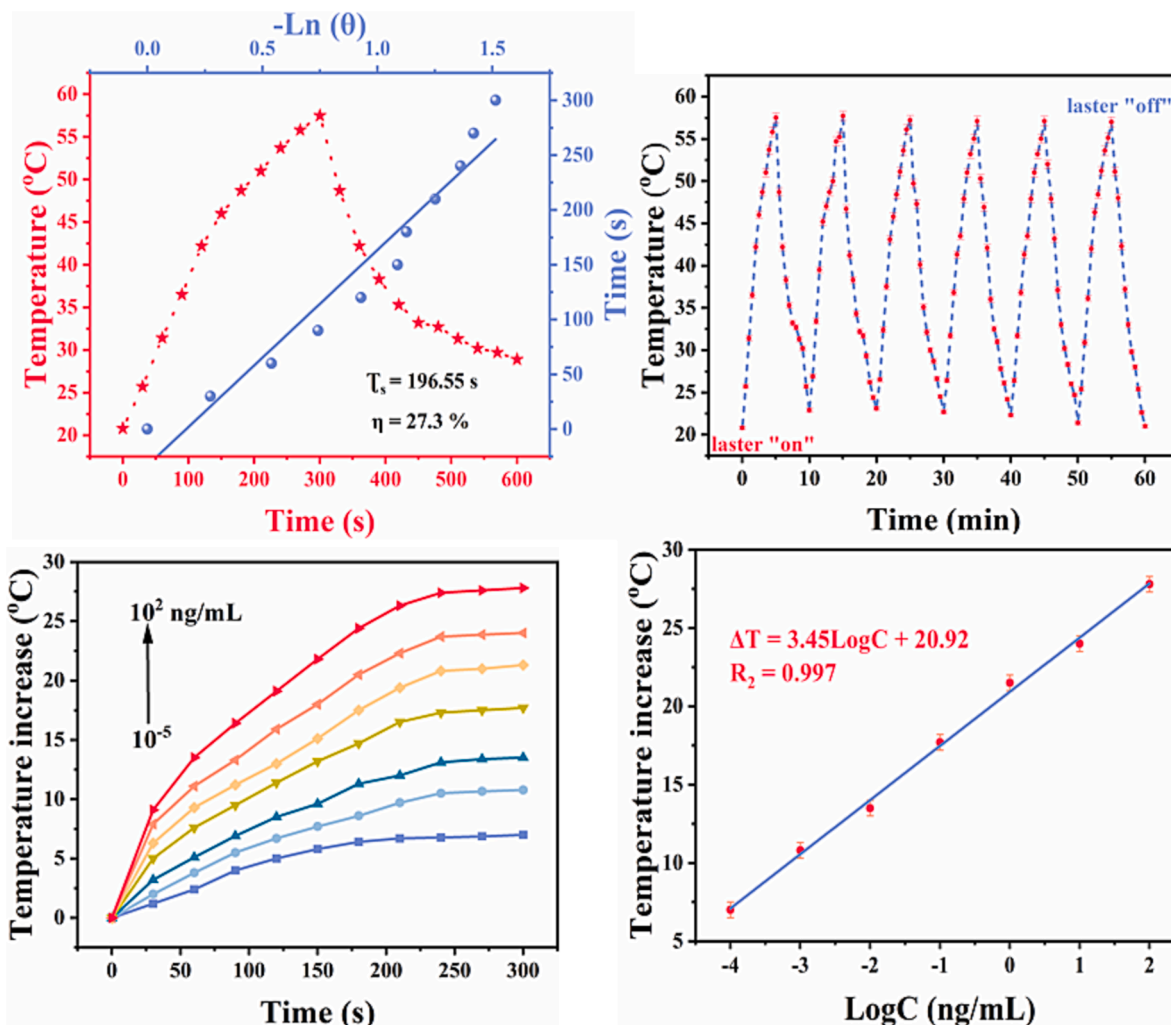
**Fig. 8.** (a) Calculation of η and (b) photothermal stability over six laser-on/off cycles of BOB/ZFO-GO(2); (c) temperature increase (ΔT) of different concentrations ($10^{-4}$, $10^{-3}$, $10^{-2}$, $10^{-1}$, $10^{0}$, 10 and $10^{2}$ ng/mL) of TC in photothermal detection system based on Apt-modified BOB/ZFO-GO(2) irradiated with an 808 nm laser at 1.5 W cm$^{-2}$ for 300 s and (d) the corresponding calibration plots for TC detection.
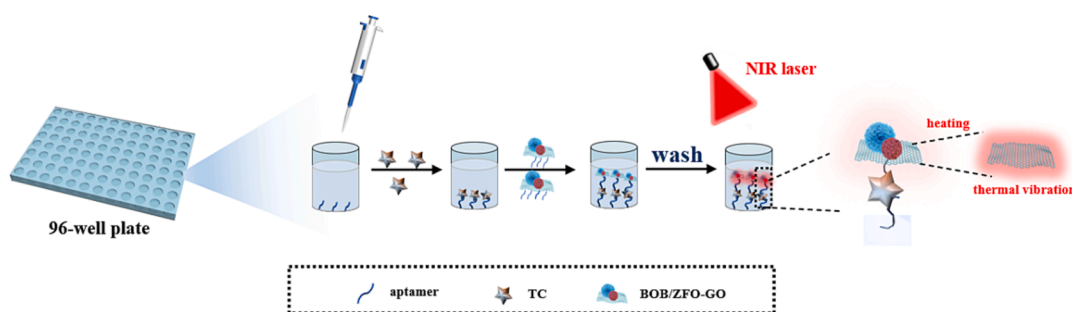


**Scheme 2.** Schematic diagram of Apt-modified BOB/ZFO-GO(2) NCs for TC photothermal detection.

(2)-based photothermal sensor can achieve photothermal detection of TC with a low detection limit of $10^{-4}$ ng/mL.

## 4. Conclusions

In summary, a novel magnetically recoverable multifunctional BOB/ZFO-GO S-scheme heterojunction with both efficient photocatalytic degradation and trace detection for TC was successfully synthesized. Firstly, BOB/ZFO S-scheme heterostructure was constructed by ordinary hydrothermal method, and a reasonable electron transfer path was proposed by radical capture experiments. By adjusting the amount of GO addition in BOB/ZFO-GO NCs, the best degradation for TC was achieved when GO was at a mass content of 2 wt% (BOB/ZFO-GO(2)). The introduction of GO expanded the light absorption of the photocatalyst from the visible region to the NIR region. When the photocatalyst was exposed to NIR light radiation, the photothermal effect of GO could produce local heat and speed up the electron transfer between BiOBr and ZnFe$_2$O$_4$ nanocrystals, which facilitated the photocatalytic degradation efficiency. Meanwhile, the separation efficiency of photogenerated carriers was significantly enhanced through constructing S-scheme

heterojunction, and the photocatalytic-photothermal synergy achieved the efficient elimination for TC. Under visible/NIR light, TC was almost completely degraded within 80 min. Moreover, it was determined that the BOB/ZFO-GO(2) had a photothermal conversion efficiency of 23%, which was comparable to photocatalyst made of precious metals. Subsequently, the Apt-modified BOB/ZFO-GO NCs were connected to TC molecules to construct a sandwich-type photothermal detection sensor with a detection limit as low as $10^{-4}$ ng/mL. And there was a clear linear correlation between temperature increase and TC concentration in the range from $10^{-4}$ to $10^{2}$ ng/mL. BOB/ZFO-GO NCs could be recycled, and their photocatalytic and photothermal properties were stable even after several cycles. In addition to providing a brand-new method for creating a superb multifunctional photocatalyst for degradation, antibiotic concentration detection and magnetic separation recovery, this work has significant potential for safeguarding the environment and public health.

## CRediT authorship contribution statement

**Sicheng Cui:** Writing – original draft. **Yuan Cong:** Investigation. **Wenshi Zhao:** Formal analysis. **Rui Guo:** Formal analysis. **Xiaohan Wang:** Conceptualization. **Bohui Lv:** Data curation. **Hongbo Liu:** Visualization. **Yang Liu:** Supervision. **Qi Zhang:** Validation.

## Declaration of Competing Interest

The authors declare that they have no known competing financial interests or personal relationships that could have appeared to influence the work reported in this paper.

## Data availability

Data will be made available on request.

## Acknowledgments

## Appendix A. Supplementary material

Supplementary data to this article can be found online at https://doi.org/10.1016/j.jcis.2023.10.051.

## References

[1] H. Feng, J. Yu, J. Tang, L. Tang, Y. Liu, Y. Lu, J. Wang, T. Ni, Y. Yang, Y. Yi, Enhanced electro-oxidation performance of FeCoLDH to organic pollutants using hydrophilic structure, J. Hazard. Mater. 430 (2022), 128464.

[2] M. Kong, Y.-Q. Bu, Q. Zhang, S.-H. Zhang, L.-Q. Xing, Z.-Q. Gao, F.-Z. Bi, G.-J. Hu, Distribution, abundance, and risk assessment of selected antibiotics in a shallow freshwater body used for drinking water, China, J. Environ. Manage. 280 (2021), 111738.

[3] S. Sengupta, M.K. Chattopadhyay, H.-P. Grossart, The multifaceted roles of antibiotics and antibiotic resistance in nature, Front. Microbiol. 4 (2013).

[4] Y. Li, S. Shu, L. Huang, J. Liu, J. Liu, J. Yao, S. Liu, M. Zhu, L. Huang, Construction of a novel double S-scheme structure WO₃/g-C₃N₄/BiOI: Enhanced photocatalytic performance for antibacterial activity, J. Colloid Interface Sci. 633 (2023) 60–71.

[5] D. Brown, Antibiotic resistance breakers: can repurposed drugs fill the antibiotic discovery void, Nat. Rev. Drug Discovery. 14 (2015) 821–832.

[6] T. Zhu, Z. Su, W. Lai, Y. Zhang, Y. Liu, Insights into the fate and removal of antibiotics and antibiotic resistance genes using biological wastewater treatment technology, Sci. Total Environ. 776 (2021), 145906.

[7] Q. Chen, H. Zhou, J. Wang, J. Bi, F. Dong, Activating earth-abundant insulator BaSO₄ for visible-light induced degradation of tetracycline, Appl. Catal. B-Environ. 307 (2022), 121182.

[8] J. Liu, H. He, Z. Shen, H.H. Wang, W. Li, Photoassisted highly efficient activation of persulfate over a single-atom Cu catalyst for tetracycline degradation: Process and mechanism, J. Hazard. Mater. 429 (2022), 128398.

[9] P. Guo, F. Zhao, X. Hu, Boron- and europium-co-doped g-C₃N₄ nanosheets: Enhanced photocatalytic activity and reaction mechanism for tetracycline degradation, Ceram. Int. 47 (2021) 16256–16268.

[10] X. Hu, Y. Zhao, J. Dong, C. Liu, Y. Qi, G. Fang, S. Wang, A strong blue fluorescent nanoprobe based on Mg/N co-doped carbon dots coupled with molecularly imprinted polymer for ultrasensitive and highly selective detection of tetracycline in animal-derived foods, Sensor. Actuat. B-Chem. 338 (2021), 129809.

[11] C. Hong, X. Zhang, S. Ye, H. Yang, Z. Huang, D. Yang, R. Cai, W. Tan, Aptamer-Pendant DNA Tetrahedron Nanostructure Probe for Ultrasensitive Detection of Tetracycline by Coupling Target-Triggered Rolling Circle Amplification, ACS Appl. Mater. Interfaces. 13 (2021) 19695–19700.

[12] A.O. Egbedina, K.O. Adebowale, B.I. Olu-Owolabi, E.I. Unuabonah, M.O. Adesina, Green synthesis of ZnO coated hybrid biochar for the synchronous removal of ciprofloxacin and tetracycline in wastewater, RSC Adv. 11 (2021) 18483–18492.

[13] Z. Zha, J. Lai, Y. Li, J. Yang, S. Cui, Y. Li, The degradation of tetracycline by modified BiOCl nanosheets with carbon dots from the chlorella, J. Alloys Compd. 855 (2021), 157454.

[14] X. Wang, G. Xu, Y. Tu, D. Wu, A. Li, X. Xie, BiOBr/PBCD-B-D dual-function catalyst with oxygen vacancies for Acid Orange 7 removal: Evaluation of adsorption-photocatalysis performance and synergy mechanism, Chem. Eng. J. 411 (2021), 128456.

[15] G.-Y. Wang, S.-S. Yang, J. Ding, C.-X. Chen, L. Zhong, L. Ding, M. Ma, G.-S. Sun, Z.-L. Huang, N.-Q. Ren, Immobilized redox mediators on modified biochar and their role on azo dye biotransformation in anaerobic biological systems: Mechanisms, biodegradation pathway and theoretical calculation, Chem. Eng. J. 423 (2021), 130300.

[16] S.A. Ismail, W.L. Ang, A.W. Mohammad, Electro-Fenton technology for wastewater treatment: A bibliometric analysis of current research trends, future perspectives and energy consumption analysis, J. Water Process Eng. 40 (2021), 101952.

[17] Y. Shang, C. Wang, C. Yan, F. Jing, M. Roostaeinia, Y. Wang, G. Chen, C. Lv, An efficient and multifunctional S-scheme heterojunction photocatalyst constructed by tungsten oxide and graphitic carbon nitride: Design and mechanism study, J. Colloid Interface Sci. 634 (2023) 195–208.

[18] C. Liu, S. Mao, H. Wang, Y. Wu, F. Wang, M. Xia, Q. Chen, Peroxymonosulfate-assisted for facilitating photocatalytic degradation performance of 2D/2D WO₃/BiOBr S-scheme heterojunction, Chem. Eng. J. 430 (2022), 132806.

[19] M. Kaur, S.K. Mehta, P. Devi, S.K. Kansal, Bi₂WO₆/NH₂-MIL-88B(Fe) heterostructure: An efficient sunlight driven photocatalyst for the degradation of antibiotic tetracycline in aqueous medium, Adv. Powder Technol. 32 (2021) 4788–4804.

[20] T. Wu, Q. He, Z. Liu, B. Shao, Q. Liang, Y. Pan, J. Huang, Z. Peng, Y. Liu, C. Zhao, X. Yuan, L. Tang, S. Gong, Tube wall delamination engineering induces photogenerated carrier separation to achieve photocatalytic performance improvement of tubular g-C₃N₄, J. Hazard. Mater. 424 (2022), 127177.

[21] H. Zhou, W. Qu, M. Wu, Z. Yuan, J. Jian, L. Zhang, T. Huang, Synthesis of novel BiOBr/Bio-veins composite for photocatalytic degradation of pollutants under visible-light, Surf. Interfaces 28 (2022), 101668.

[22] Z. Miao, Q. Wang, Y. Zhang, L. Meng, X. Wang, In situ construction of S-scheme AgBr/BiOBr heterojunction with surface oxygen vacancy for boosting photocatalytic CO₂ reduction with H₂O, Appl. Catal. B-Environ. 301 (2022), 120802.

[23] G. Peng, Y. Xie, Y. Wang, Q. Yu, Y. Huang, S. Liu, L. Lu, Triggering sustainable regeneration of Fe2+ by S-scheme Bi₂Fe₄O₉/BiOBr heterojunction toward highly efficient peroxymonosulfate activation for visible-light-driven removal of thiabendazole, Appl. Surf. Sci. 631 (2023), 157567.

[24] K. Perumal, S. Shanavas, T. Ahamad, A. Karthigeyan, P. Murugakoothan, Construction of Ag₂CO₃/BiOBr/CdS ternary composite photocatalyst with improved visible-light photocatalytic activity on tetracycline molecule degradation, J. Environ. Sci. 125 (2023) 47–60.

[25] L. Jiang, Y. Xie, F. He, Y. Ling, J. Zhao, H. Ye, S. Li, J. Wang, Y. Hou, Facile synthesis of GO as middle carrier modified flower-like BiOBr and C₃N₄ nanosheets for simultaneous treatment of chromium(VI) and tetracycline, Chin. Chem. Lett. 32 (2021) 2187–2191.

[26] F. Zheng, H. Lu, M. Guo, M. Zhang, Q. Zhen, Hydrothermal preparation of WO₃ nanorod array and ZnO nanosheet array composite structures on FTO substrates with enhanced photocatalytic properties, J. Mater. Chem. C. 3 (2015) 7612–7620.

[27] J.-C. Sin, S.-M. Lam, H. Zeng, H. Lin, H. Li, A.R. Mohamed, Constructing magnetic separable BiOBr/MnFe₂O₄ as efficient Z-scheme nanocomposite for visible light-driven degradation of palm oil mill effluent and inactivation of bacteria, Mater. Lett. 275 (2020), 128112.

[28] Y. Zhou, W. Jiao, Y. Xie, F. He, Y. Ling, Q. Yang, J. Zhao, H. Ye, Y. Hou, Enhanced photocatalytic CO₂-reduction activity to form CO and CH₄ on S-scheme heterostructured ZnFe₂O₄/Bi₂MoO₆ photocatalyst, J. Colloid Interface Sci. 608 (2022) 2213–2223.

[29] H. Guo, H.-Y. Niu, C. Liang, C.-G. Niu, D.-W. Huang, L. Zhang, N. Tang, Y. Yang, C.-Y. Feng, G.-M. Zeng, Insight into the energy band alignment of magnetically separable Ag₂O/ZnFe₂O₄ p-n heterostructure with rapid charge transfer assisted visible light photocatalysis, J. Catal. 370 (2019) 289–303.

[30] Y. Zhang, J. Di, X. Zhu, M. Ji, C. Chen, Y. Liu, L. Li, T. Wei, H. Li, J. Xia, Chemical bonding interface in Bi₂Sn₂O₇/BiOBr S-scheme heterojunction triggering efficient N₂ photofixation, Appl. Catal. B-Environ. 323 (2023), 122148.

[31] Q. Niu, Q. Chen, G. Huang, L. Li, Y. He, J. Bi, Build-in electric field in CuWO₄/covalent organic frameworks S-scheme photocatalysts steer boosting charge

transfer for photocatalytic $CO_2$ reduction, J. Colloid Interface Sci. 643 (2023) 102–114.

[32] Y. Wang, L. Ding, C. Liu, Y. Lu, Q. Wu, C. Wang, Q. Hu, 0D/2D/2D $ZnFe_2O_4$/$Bi_2O_2CO_3$/BiOBr double Z-scheme heterojunctions for the removal of tetracycline antibiotics by permonosulfate activation: Photocatalytic and non-photocatalytic mechanisms, radical and non-radical pathways, Sep. Purif. Technol. 283 (2022), 120164.

[33] M. Chen, Y. Dai, J. Guo, H. Yang, D. Liu, Y. Zhai, Solvothermal synthesis of biochar@$ZnFe_2O_4$/BiOBr Z-scheme heterojunction for efficient photocatalytic ciprofloxacin degradation under visible light, Appl. Surf. Sci. 493 (2019) 1361–1367.

[34] B. Li, Y. Hu, Z. Shen, Z. Ji, L. Yao, S. Zhang, Y. Zou, D. Tang, Y. Qing, S. Wang, G. Zhao, X. Wang, Photocatalysis Driven by Near-Infrared Light: Materials Design and Engineering for Environmentally Friendly Photoreactions, ACS EST Engg. 1 (2021) 947–964.

[35] Z. Jia, C. Yuan, Y. Liu, X.-J. Wang, P. Sun, L. Wang, H. Jiang, J. Jiang, Strategies to approach high performance in $Cr^{3+}$-doped phosphors for high-power NIR-LED light sources, Light-Sci. Appl. 9 (2020) 86.

[36] S. Kargar, S. Khoei, S. Khoee, S. Shirvalilou, S.R. Mahdavi, Evaluation of the combined effect of NIR laser and ionizing radiation on cellular damages induced by IUdR-loaded PLGA-coated Nano-graphene oxide, Photodiagnosis and Photodynamic Ther. 21 (2018) 91–97.

[37] Y.-S. Guan, Y. Qiao, Y. Liang, H.K. Bisoyi, C. Wang, W. Xu, D. Zhu, Q. Li, A high mobility air-stable n-type organic small molecule semiconductor with high UV–visible-to-NIR photoresponse, Light-Sci. Appl. 11 (2022) 236.

[38] N. Lv, Y. Li, Z. Huang, T. Li, S. Ye, D.D. Dionysiou, X. Song, Synthesis of GO/$TiO_2$/$Bi_2WO_6$ nanocomposites with enhanced visible light photocatalytic degradation of ethylene, Appl. Catal. B-Environ. 246 (2019) 303–311.

[39] W. Yang, M. Pan, C. Huang, Z. Zhao, J. Wang, H. Zeng, Graphene oxide-based noble-metal nanoparticles composites for environmental application, Compos. Commun. 24 (2021), 100645.

[40] Z. Li, H. Lei, A. Kan, H. Xie, W. Yu, Photothermal applications based on graphene and its derivatives: A state-of-the-art review, Energy. 216 (2021), 119262.

[41] P. Qiu, N. Xue, Z. Cheng, X. Kai, Y. Zeng, M. Xu, S. Zhang, C. Xu, F. Liu, Z. Guo, The cooperation of photothermal conversion, photocatalysis and sulfate radical-based advanced oxidation process on few-layered graphite modified graphitic carbon nitride, Chem. Eng. J. 417 (2021), 127993.

[42] S. Lahouidak, M.L. Soriano, R. Salghi, M. Zougagh, Á. Ríos, Graphene quantum dots for enhancement of fluorimetric detection coupled to capillary electrophoresis for detection of ofloxacin, ELECTROPHORESIS. (2019) elps.201900037.

[43] M. Hu, Y. Ben, M.H. Wong, C. Zheng, Trace Analysis of Multiclass Antibiotics in Food Products by Liquid Chromatography-Tandem Mass Spectrometry: Method Development, J. Agric. Food Chem. 69 (2021) 1656–1666.

[44] X. Wang, J. Li, D. Jian, Y. Zhang, Y. Shan, S. Wang, F. Liu, Paper-based antibiotic sensor (PAS) relying on colorimetric indirect competitive enzyme-linked immunosorbent assay for quantitative tetracycline and chloramphenicol detection, Sensor. Actuat. B-Chem. 329 (2021), 129173.

[45] F. Li, Y. Wu, D. Chen, Y. Guo, X. Wang, X. Sun, Sensitive dual-labeled electrochemical aptasensor for simultaneous detection of multi-antibiotics in milk, Int. J. Hydrogen Energy 46 (2021) 23301–23309.

[46] X. Wang, J. Zeng, Q. Sun, J. Yang, Y. Xiao, Z. Zhu, B. Yan, Y. Li, An effective method towards label-free detection of antibiotics by surface-enhanced Raman spectroscopy in human serum, Sensor. Actuat. B-Chem. 343 (2021) 130084.

[47] B. Liu, S. Zheng, H. Li, J. Xu, H. Tang, Y. Wang, Y. Wang, F. Sun, X. Zhao, Ultrasensitive and facile detection of multiple trace antibiotics with magnetic nanoparticles and core-shell nanostar SERS nanotags, Talanta. 237 (2022), 122955.

[48] K.Y. Lau, J. Qiu, Broad applications of sensors based on laser-scribed graphene, Light-Sci. Appl. 12 (2023) 168.

[49] L. Su, Y. Chen, L. Wang, H. Zhang, J. Sun, J. Wang, D. Zhang, Dual-signal based immunoassay for colorimetric and photothermal detection of furazolidone, Sensor. Actuat. B-Chem. 331 (2021), 129431.

[50] X. Li, S. Lu, X. Mu, T. Li, S. Sun, Y. Zhao, J. Hai, B. Wang, Red-light-responsive coordination polymers nanorods: New strategy for ultrasensitive photothermal detection of targeted cancer cells, Biosens. Bioelectron. 190 (2021) 113417.

[51] T. Dai, Y. Wan, R. Tian, S. Wang, T. Han, G. Wang, In Situ Cation Exchange Generated ZnS-$Ag_2S$ Nanoparticles for Photothermal Detection of Transcription Factor, ACS Appl. Bio Mater. 3 (2020) 3260–3267.

[52] J. Wang, C. Chong, C. Hong, Z. Lin, Z. Huang, Rapid detection of malachite green in fish and water based on the peroxidase-like activity of $Fe_3O_4$ NPs enhanced with aptamer, J. Food Compos. Anal. 104 (2021), 104162.

[53] T. Zhao, Q. Chen, Y. Wen, X. Bian, Q. Tao, G. Liu, J. Yan, A competitive colorimetric aptasensor for simple and sensitive detection of kanamycin based on terminal deoxynucleotidyl transferase-mediated signal amplification strategy, Food Chem. 377 (2022), 132072.

[54] W. Zhao, D. Zhang, T. Zhou, J. Huang, Y. Wang, B. Li, L. Chen, J. Yang, Y. Liu, Aptamer-conjugated magnetic $Fe_3O_4$@Au core-shell multifunctional nanoprobe: A three-in-one aptasensor for selective capture, sensitive SERS detection and efficient near-infrared light triggered photothermal therapy of Staphylococcus aureus, Sensor. Actuat. B-Chem. 350 (2022), 130879.

[55] P. Qin, Y. Guan, Y. Qiu, Novel Photothermal Aptamer-based Sensing System for Highly Ultrasensitive Detection of Ochratoxin A, Sens. Mater. 33 (2021) 3635.

[56] M. Yüce, N. Ullah, H. Budak, Trends in aptamer selection methods and applications, Analyst. 140 (2015) 5379–5399.

[57] Z. Zhang, Y. Tian, P. Huang, F.-Y. Wu, Using target-specific aptamers to enhance the peroxidase-like activity of gold nanoclusters for colorimetric detection of tetracycline antibiotics, Talanta. 208 (2020), 120342.

[58] W. Zhao, S. Yang, D. Zhang, T. Zhou, J. Huang, M. Gao, Y. Jiang, Y. Liu, J. Yang, Ultrasensitive dual-enhanced sandwich strategy for simultaneous detection of Escherichia coli and Staphylococcus aureus based on optimized aptamers-functionalized magnetic capture probes and graphene oxide-Au nanostars SERS tags, J. Colloid Interface Sci. 634 (2023) 651–663.

[59] C. Liang, J. Song, Y. Zhang, Y. Guo, M. Deng, W. Gao, J. Zhang, Facile Approach to Prepare rGO@$Fe_3O_4$ Microspheres for the Magnetically Targeted and NIR-responsive Chemo-photothermal Combination Therapy, Nanoscale Res. Lett. 15 (2020) 86.

[60] L. Zheng, W. Dong, C. Zheng, Y. Shen, R. Zhou, Z. Wei, Z. Chen, Y. Lou, Rapid photothermal detection of foodborne pathogens based on the aggregation of MPBA-AuNPs induced by MPBA using a thermometer as a readout, Colloid Surface B 212 (2022), 112349.

[61] S.H. Jalalian, N. Karimabadi, M. Ramezani, K. Abnous, S.M. Taghdisi, Electrochemical and optical aptamer-based sensors for detection of tetracyclines, Trends Food Sci. Tech. 73 (2018) 45–57.

[62] Z. Fang, L. Zhang, H. Qi, H. Yue, T. Zhang, X. Zhao, G. Chen, Y. Wei, C. Wang, D. Zhang, Nanosheet assembled hollow $ZnFe_2O_4$ microsphere as anode for lithium-ion batteries, J. Alloy Compd. 762 (2018) 480–487.

[63] M. Zhang, X. Xie, Y. Si, J. Gao, H. Du, S. Pei, X. Zhang, Q. Yan, Enhanced photocatalytic performance of $ZnFe_2O_4$/BiOI hybrid for the degradation of methyl orange, J. Mater. Sci-Mater. El. 30 (2019) 8055–8063.

[64] D.C. Marcano, D.V. Kosynkin, J.M. Berlin, A. Sinitskii, Z. Sun, A. Slesarev, L. B. Alemany, W. Lu, J.M. Tour, Improved Synthesis of Graphene Oxide, ACS Nano 4 (2010) 4806–4814.

[65] S.K. Vashist, Comparison of 1-Ethyl-3-(3-Dimethylaminopropyl) Carbodiimide Based Strategies to Crosslink Antibodies on Amine-Functionalized Platforms for Immunodiagnostic Applications, Diagnostics 2 (2012) 23–33.

[66] Y. Wei, D. Wang, Y. Zhang, J. Sui, Z. Xu, Multicolor and photothermal dual-readout biosensor for visual detection of prostate specific antigen, Biosens. Bioelectron. 140 (2019), 111345.

[67] M. Huang, J. Yu, Q. Hu, W. Su, M. Fan, B. Li, L. Dong, Preparation and enhanced photocatalytic activity of carbon nitride/titania (001 vs 101 facets)/reduced graphene oxide (g-$C_3N_4$/$TiO_2$/rGO) hybrids under visible light, Appl. Surf. Sci. 389 (2016) 1084–1093.

[68] M. Wang, Z. Ai, L. Zhang, Generalized Preparation of Porous Nanocrystalline $ZnFe_2O_4$ Superstructures from Zinc Ferrioxalate Precursor and Its Superparamagnetic Property, J. Phys. Chem. C 112 (2008) 13163–13170.

[69] J. Yue, G. Wen, G. Ren, S. Tang, B. Ge, L. Zhao, X. Shao, Superhydrophobic Self-Supporting BiOBr Aerogel for Wastewater Purification, Langmuir. 37 (2021) 406–416.

[70] Y. Zhu, W. Ding, J. Li, J. Zhang, Synthesis of enhanced visible-light-driven and magnetic recoverable photocatalyst by immobilizing $ZnFe_2O_4$-BiOBr heterojunctions onto palygorskite surface, Mater. Res. Express. 6 (2019), 085547.

[71] R. Zhang, Y. Li, Q. Han, T. Zhang, Y. Liu, K. Zeng, C. Zhao, Investigation the High Photocatalytic Activity of Magnetically Separable Graphene Oxide Modified BiOBr Nanocomposites for Degradation of Organic Pollutants and Antibiotic, J. Inorg. Organomet. Polym. Mater. 30 (2020) 1703–1715.

[72] Y. Yang, H. Yin, H. Li, Q. Zou, Z. Zhang, W. Pei, L. Luo, Y. Huo, H. Li, Synergistic Photocatalytic-Photothermal Contribution to Antibacterial Activity in BiOI-Graphene Oxide Nanocomposites, ACS Appl. Bio Mater. 1 (2018) 2141–2152.

[73] L. Gan, H. Guo, Z. Wang, X. Li, W. Peng, J. Wang, S. Huang, M. Su, A facile synthesis of graphite/silicon/graphene spherical composite anode for lithium-ion batteries, Electrochim. Acta 104 (2013) 117–123.

[74] H. Li, F. Deng, Y. Zheng, L. Hua, C. Qu, X. Luo, Visible-light-driven Z-scheme rGO/$Bi_2S_3$-BiOBr heterojunctions with tunable exposed BiOBr (102) facets for efficient synchronous photocatalytic degradation of 2-nitrophenol and Cr(vi) reduction, Environ. Sci-Nano 6 (2019) 3670–3683.

[75] W. Liu, Y. Gao, Y. Yang, Q. Zou, G. Yang, Z. Zhang, H. Li, Y. Miao, H. Li, Y. Huo, Photocatalytic Composite of a Floating BiOBr@Graphene Oxide@Melamine Foam for Efficient Removal of Organics, ChemCatChem. 10 (2018) 2394–2400.

[76] M. Zheng, X. Ma, J. Hu, X. Zhang, D. Li, W. Duan, Novel recyclable BiOBr/$Fe_3O_4$/RGO composites with remarkable visible-light photocatalytic activity, RSC Adv. 10 (2020) 19961–19973.

[77] L. Yosefi, M. Haghighi, S. Allahyari, Solvothermal synthesis of flowerlike p-BiOI/n-$ZnFe_2O_4$ with enhanced visible light driven nanophotocatalyst used in removal of acid orange 7 from wastewater, Sep. Purif. Technol. 178 (2017) 18–28.

[78] S. Guan, H. Yang, X. Sun, T. Xian, Preparation and promising application of novel $LaFeO_3$/BiOBr heterojunction photocatalysts for photocatalytic and photo-Fenton removal of dyes, Opt. Mater. 100 (2020), 109644.

[79] D. Lee, S. So, G. Hu, M. Kim, T. Badloe, H. Cho, J. Kim, H. Kim, C.-W. Qiu, J. Rho, Hyperbolic metamaterials: fusing artificial structures to natural 2D materials, eLight 2 (2022) 1.

[80] H. Yu, H. Huang, K. Xu, W. Hao, Y. Guo, S. Wang, X. Shen, S. Pan, Y. Zhang, Liquid Phase Exfoliation into Monolayered BiOBr Nanosheets for Photocatalytic Oxidation and Reduction, ACS Sustainable Chem. Eng. 11 (2017) 10499–10508.

[81] T. Li, J. Liu, F. Shi, X. Song, H. Zhang, H. Zhang, C. Ma, K. Zhu, J. Liu, Construction of a novel highly porous BiOBr/$CsxWO_3$@$SiO_2$ composite aerogel: Adsorption/self-heating photocatalytic synergistic degradation of antibiotics and mechanism study, J. Environ. Chem. Eng. 10 (2022), 107785.

[82] P. Sarkar, S. De, S. Neogi, Microwave assisted facile fabrication of dual Z-scheme g-$C_3N_4$/$ZnFe_2O_4$/$Bi_2S_3$ photocatalyst for peroxymonosulphate mediated degradation

of 2,4,6-Trichlorophenol: The mechanistic insights, Appl. Catal. B-Environ. 307 (2022), 121165.

[83] J. Zhang, H. Tong, W. Pei, W. Liu, F. Shi, Y. Li, Y. Huo, Integrated photocatalysis-adsorption-membrane separation in rotating reactor for synergistic removal of RhB, Chemosphere. 270 (2021), 129424.

[84] J. Huang, T. Zhou, W. Zhao, S. Cui, R. Guo, D. Li, N. Reddy Kadasala, D. Han, Y. Jiang, Y. Liu, H. Liu, Multifunctional magnetic $Fe_3O_4/Cu_2O$-Ag nanocomposites with high sensitivity for SERS detection and efficient visible light-driven photocatalytic degradation of polycyclic aromatic hydrocarbons (PAHs), J. Colloid Interface Sci. 628 (2022) 315–326.

[85] J.-C. Sin, S.-M. Lam, H. Zeng, H. Lin, H. Li, A. Kugan Kumaresan, A.R. Mohamed, J.-W. Lim, Z-scheme heterojunction nanocomposite fabricated by decorating magnetic $MnFe_2O_4$ nanoparticles on BiOBr nanosheets for enhanced visible light photocatalytic degradation of 2,4-dichlorophenoxyacetic acid and Rhodamine B, Sep. Purif. Technol. 250 (2020), 117186.

[86] Y. Li, Z. Lai, Z. Huang, H. Wang, C. Zhao, G. Ruan, F. Du, Fabrication of BiOBr/$MoS_2$/graphene oxide composites for efficient adsorption and photocatalytic removal of tetracycline antibiotics, Appl. Surf. Sci. 550 (2021), 149342.

[87] Y.-Y. Yang, H.-P. Feng, C.-G. Niu, D.-W. Huang, H. Guo, C. Liang, H.-Y. Liu, S. Chen, N. Tang, L. Li, Constructing a plasma-based Schottky heterojunction for near-infrared-driven photothermal synergistic water disinfection: Synergetic effects and antibacterial mechanisms, Chem. Eng. J. 426 (2021), 131902.

[88] H. Feng, J. Yu, L. Tang, J. Wang, H. Dong, T. Ni, J. Tang, W. Tang, X. Zhu, C. Liang, Improved hydrogen evolution activity of layered double hydroxide by optimizing the electronic structure, Appl. Catal. B-Environ. 297 (2021), 120478.

[89] H.-Y. Liu, C.-G. Niu, D.-W. Huang, C. Liang, H. Guo, Y.-Y. Yang, L. Li, Unravelling the role of reactive oxygen species in ultrathin Z-scheme heterojunction with surface zinc vacancies for photocatalytic $H_2O_2$ generation and CTC degradation, Chem. Eng. J. 465 (2023), 143007.

[90] P. Qiu, Z. Cheng, N. Xue, Y. Zeng, X. Kai, S. Zhang, C. Xu, F. Liu, Z. Guo, The synergistic effect in metal-free graphene oxide coupled graphitic carbon nitride/light/peroxymonosulfate system: Photothermal effect and catalyst stability, Carbon 178 (2021) 81–91.